An efficient two-way coupling approach for viscous and potential flows in free-surface hydrodynamic simulations

Kaiyuan Shi[a,d], Xin Lu[b,*], Dao My Ha[b], Yulong Li[c], Renchuan Zhu[a]

[a]*State Key Laboratory of Ocean Engineering, School of Ocean and Civil Engineering, Shanghai Jiao Tong University, Shanghai, 200240, China*

[b]*Department of Fluid Mechanics, Institute of High Performance Computing (IHPC), Agency for Science, Technology and Research (A*STAR), 1 Fusionopolis Wy, #16-16 Connexis, North Tower, Singapore*

[c]*Technology Centre for Offshore and Marine, Singapore (TCOMS), 118411, Singapore*

[d]*Yazhou Bay Institute of Deepsea Technology, Shanghai Jiao Tong University, Sanya, 572000, China*

Abstract

This paper presents a novel two-way coupling strategy between viscous and potential flows, termed the Spectral Coupling Layer (SCL) method. This approach integrates a locally resolved viscous region, simulated via OpenFOAM (OF), within a global potential-flow domain solved by the High-Order Spectral (HOS) method. Coupling the pseudo-spectral HOS formulation with time-domain viscous solvers is non-trivial. To address this, the SCL method employs a free-surface velocity-potential correction to transfer flow information from the viscous region to the potential field. A virtual disturbance layer is constructed by sampling velocities from the viscous solution and integrating them directly into the HOS field without iterative matching. Furthermore, a dedicated sampling strategy is introduced to eliminate spurious free-surface velocities inherent to the viscous solver. The proposed approach is validated against pure HOS simulations of wave propagation in two- and three-dimensional domains and demonstrated using a KRISO container ship advancing in calm water. Results indicate that the method achieves high computational accuracy while offering superior flexibility and applicability for complex coastal and marine engineering problems.

Keywords: Two-way coupling, Viscous–potential flow coupling, High-order spectral, OpenFOAM, Wave–structure interaction, Computational fluid dynamics

1 Introduction

In the field of ocean engineering, the accurate prediction of complex fluid behaviors, particularly the nonlinear evolution of ocean waves and wave-structure interactions, is critical for assessing the safety and operational efficiency of marine structures. With the rapid advancement of computational fluid dynamics (CFD), numerical simulations based on the Navier-Stokes (N-S) equations have become robust tools for resolving fine flow structures and nonlinear hydrodynamic characteristics. These methods are widely applied to investigate phenomena such as gap resonance (Gao et al., 2024; Gong et al., 2024; Gong et al., 2025; Mi et al., 2025a; Mi et al., 2025b; Gao et al., 2026), hydrodynamic resistance (Li et al., 2012; Luo et al., 2022; Deng et al., 2024), vortex-induced vibrations (Li et al., 2018a; Zhang et al., 2020), and wave-structure-interaction(Chen et al., 2025; Guo et al., 2025). However, while N-S solvers demonstrate superior capability in capturing fluid viscosity and strong nonlinearities, handling free-surface flows

* Corresponding author. E-mail: lux@a-star.edu.sg

remains a challenge. Traditional interface capturing techniques, such as the Volume of Fluid (VOF) and Level Set (LS) methods, typically require refined meshes near the free surface. This requirement leads to a substantial increase in computational costs and often encounters difficulties regarding numerical dissipation and mass conservation during long-distance wave simulations (Lin, 2008).

In contrast, potential flow theory offers a computationally efficient alternative for large-scale wave evolution. Assuming the fluid is inviscid, incompressible, and irrotational, this theory simplifies the governing equations to the Laplace equation, significantly reducing computational complexity. Potential flow models are extensively used for ship seakeeping analysis and motion prediction of large floating structures where viscous effects are not important (Li et al., 2019; Tang et al., 2021). The primary advantage of this approach lies in its ability to accurately model wave propagation with minimal numerical dissipation. However, the inherent inviscid assumption prevents the description of flow separation and viscous damping effects.

To bridge the gap between efficiency and accuracy, the viscous-potential coupled method has emerged as a promising strategy. Employing domain decomposition, this approach utilizes potential flow in the far field for efficient wave propagation and solves the N-S equations in the near field to resolve complex viscous details. This hybrid strategy avoids the prohibitive costs of full-domain N-S simulations while overcoming the physical limitations of potential flow, offering an optimal balance for simulating wave-structure interactions.

The coupling between viscous and potential flow solvers could be one-way or two-way. One-way methods transmit potential flow information in a single direction through velocity or domain decomposition. A well-known one-way coupling method is the Spectral Wave Explicit Navier-Stokes Equations (SWENSE) method, as reported by Ferrant et al. (2003), Zou et al. (2013), which decomposes the velocity field in the N-S equations into incident and scattered wave components. The incident wave field is explicitly calculated and treated as a known quantity using potential flow theory while the scattered wave field is solved by the N-S equations. Chen and Maki (2017) proposed a velocity decomposition method based on Helmholtz decomposition, separating the velocity field into irrotational and rotational components. The irrotational flow field is solved first using Boundary Element Method (BEM), while the rotational component is obtained from the N-S equations. Another type of one-way coupling method uses the potential flow incident wave field to provide boundary conditions for the viscous flow field. The Euler Overlay Method (EOM), proposed by Kim et al. (2012), introduces source terms into the N-S equations to guide the viscous flow field toward the potential flow solution. Similarly, the Waves2Foam module in OpenFOAM (Jacobsen et al., 2012) introduces relaxation zones at domain boundaries, allowing the viscous flow simulation to relax toward potential flow results (e.g., Ducrozet et al., 2014). Lu et al. (2022) introduced a wave-current interaction algorithm in the HOS method (Dommermuth and Yue, 1987), accelerated by using GPUs and coupled with OpenFOAM to investigate nonlinear wave-current-structure interactions.

Two-way viscous-potential flow coupling methods are more complex, as both the viscous and potential flow domains interact with each other. Early two-way coupling methods were typically limited to steady flow simulations and subsequently extended to unsteady two-dimensional (2D) simulations. Lachaume et al. (2003) coupled the BEM with the VOF method to model wave breaking on a slope. Iafrati and Campana (2003) divided the flow field into two regions: the upper region with a free surface, modeled using the LS method, and the submerged region below the free surface, modeled using Laplace equations. Kim et al. (2010) proposed a single-step prediction-correction two-way coupling method, with a BEM potential flow domain upstream of the viscous flow domain, simulating wave propagation in two dimensions. The velocity potential at the BEM domain was simply estimated from the horizontal velocity on the lateral cell boundary of the VOF calculations directly using a spline interpolation. Research on 3D

two-way coupling methods is far more limited due to complex wave interactions. Hamilton and Yeung (2011) linearized the free surface and applied the pseudo-spectral method in a cylindrical viscous flow domain with time-domain Green's functions at the boundary. Landesman et al. (2024) successfully extended the method of Kim et al. (2010) to three dimensions. In these works, single-step velocity matching between the two domains was used which will result in velocity mismatch over time. Lu et al. (2017) achieved 3D two-way coupling by iterating the viscous and potential flow domains until the boundary velocities matched.

In the two-way coupling, the viscous flow domain receives incoming wave information from the potential flow domain while simultaneously transmits the wave surface information calculated by the viscous flow solver back to the potential flow domain. This creates a challenge in sequential time-intergrate numerical simulations, as the boundary conditions for the viscous flow are influenced by the potential flow, while at the same time the potential flow boundary conditions nonlinearly depend on the viscous flow simulation. To address this challenge, most two-way coupling methods introduce control surfaces and employ iterative approaches to match the flow fields at the coupling boundaries (e.g. Lu et al., 2017). The iteration loop, however, significantly increases algorithm complexity and computational cost, especially in 3D simulations.

To overcome these limitations, we propose a computationally efficient and easy-to-implement two-way coupling technique, referred to as the Spectral Coupling Layer (SCL) method. In the SCL method, the viscous flow field is embedded within a larger high-order spectral layer, forming an integrated viscous-potential computational domain. The near-field flow is modelled by the N–S equations within the viscous region, while the far-field flow outside the viscous region are modeled by the fully nonlinear potential flow using HOS. Inspired by the overset mesh technique in the CFD field, where one or more fixed or moving overset computational domains are embedded as disturbance sources within a unified background computational domain, the novel SCL method constructs a virtual disturbance potential flow layer by sampling the velocity of the viscous flow field. This virtual layer is seamlessly integrated with the background HOS layer using a free-surface velocity potential correction, eliminating the requirements of boundary matching in traditional methods. A sampling strategy is also developed to avoid the spurious velocities at the free surface in the viscous solver. Compared with existing viscous-potential two-way coupling algorithms, the advantages of the SCL method include:

- *Simplicity and efficiency*: The method does not require iterative boundary matching while ensuring accuracy. This results in minimal additional computational overhead compared to the viscous flow field calculation before coupling, especially for fluid-structure interaction problems using overset mesh method.

- Larger potential flow computational domain: The SCL method leverages the HOS approach, achieving $O(N\log N)$ computational complexity compared to $O(N^3)$ for traditional BEM. This efficiency enables simulation of vastly larger potential flow domains at minimal computational cost, making it ideal for large-scale open ocean hydrodynamic studies.

- *Efficient wave transmissive boundary condition*: The method can accurately introduce incident waves into and efficiently transmit outgoing waves from the viscous flow field without causing non-physical boundary reflections. The size of the viscous domain could be kept minimal.

- *Easy configuration*: The viscous flow field can be embedded at any position within the potential flow field and can move freely. This is extremely convenient for fluid-structure interaction calculations where structures need to move over large areas, such as ship navigation.

- *Good scalability*: Multiple viscous flow fields can be embedded within the background high-order spectral layer. This feature makes the method highly promising for wide range of applications, such as simulating ship-wave-ship interactions and offshore floating wind farms in which each ship or wind turbine is modelled in one viscous flow field.

The remainder of this paper is organized as follows. Section 2 describes the formulation and numerical implementation of the SCL method. The governing equations for both the viscous and potential flow regions are briefly presented in §2.1. The proposed two-way coupling strategy is described in §2.2, and a description of the numerical algorithm and implementation is provided in §2.3. The proposed methodology is validated using selected benchmark cases and the numerical results are discussed in §3. The core part of validating this numerical algorithm is to evaluate its accuracy in simulating pure-wave conditions. Sections 3.1 and 3.2 examine the accuracy of SCL in a 2D vertical plane (2DV) mode using regular and in a 3D condition with regular waves. Section 3.3 simulates the navigation of the KRISO container ship (KCS) hull in calm water and compares the wave pattern generated by the ship with published experimental measurements and numerical data. Finally, §4 summarizes the performance of the proposed method and its main features.

2 Mathematical model and numerical implementation

2.1 Governing equations and solvers

2.1.1 Viscous flow region: N-S equations

The viscous flow region is governed by the incompressible N-S equations. A Cartesian coordinate system is established, with the x- and y-axes oriented horizontally and the z-axis running vertically upward. The velocity field of the fluid is represented as $\mathbf{U} = (u, v, w)^T$. Assuming the fluid is incompressible, the velocity and pressure fields are governed by the following equations:

$$\nabla \cdot \mathbf{U} = 0 \tag{1}$$

$$\frac{\partial \rho \mathbf{U}}{\partial t} + \nabla \cdot (\rho \mathbf{U}\mathbf{U}) = -\nabla p + \rho \mathbf{g} + \nabla \cdot (\mu_e \nabla \mathbf{U}) \tag{2}$$

Here, ρ denotes the fluid density, $\mathbf{g}$ is the gravitational acceleration vector, μ_e is the effective viscosity, and p is the pressure field.

The viscous flow region is simulated using OpenFOAM (Jasak, 2009). The numerical method discretizes the flow field, including both water and air, using the Finite Volume Method (FVM). The VOF technique is used to capture the interface dynamics between the two phases. To model turbulence, the unsteady RANS approach is applied. The velocity, volume fraction, and other flow field data are stored within the volumetric grid. At each time step, the PIMPLE algorithm calculates the velocity field's time derivative based on Eq. (2) and iteratively updates the pressure field until the velocity satisfies the continuity condition in Eq. (1).

2.1.2 Potential flow region: Laplace equation

Far from the structure, the water is assumed to be irrotational and fluid viscosity is neglected. Under this assumption, a velocity potential function ϕ exists, and its gradient gives the water velocity:

$$\nabla \phi = \mathbf{U} \tag{3}$$

According to the continuity equation (1), the velocity potential function satisfies the Laplace equation:

$$\nabla^2\phi = \nabla \cdot \mathbf{U} = 0 \tag{4}$$

The velocity field in this region is determined by solving the Laplace equation. As this equation is linear, the flow field is fully defined once the boundary velocity potential is known. Assuming non-overturning waves, the free-surface elevation is denoted as $\eta(x, y, t)$, and the velocity potential on this surface is $\phi^S(x, y, t) = \phi(x, y, \eta, t)$. The elevation and velocity potential of the free surface must satisfy the following kinematic and dynamic conditions (Dommermuth and Yue, 1987):

$$\begin{cases} \dfrac{\partial \eta}{\partial t} = (1 + (\nabla_{\mathbf{x}}\eta)^2)\dfrac{\partial \phi}{\partial z} - \nabla_{\mathbf{x}}\phi^S \cdot \nabla_{\mathbf{x}}\eta & \text{on } z = \eta \\ \dfrac{\partial \phi^S}{\partial t} = \dfrac{1 + (\nabla_{\mathbf{x}}\eta)^2}{2}\left(\dfrac{\partial \phi}{\partial z}\right)^2 - g\eta - \dfrac{(\nabla_{\mathbf{x}}\phi^S)^2}{2} & \text{on } z = \eta \end{cases} \tag{5}$$

where $\nabla_{\mathbf{x}} \equiv (\partial/\partial x, \partial/\partial y)$ is the horizontal gradient operator.

The velocity potential also satisfies the impermeable boundary condition at the bottom of the flow domain:

$$\frac{\partial \phi}{\partial z} = 0 \quad \text{on } z = -d \tag{6}$$

where d is the water depth.

Equations (4)–(6) form the governing equations and boundary conditions for the potential flow field. In Eq. (5), given η and ϕ^S, it is sufficient to compute the horizontal derivatives $\nabla_{\mathbf{x}}\eta$, $\nabla_{\mathbf{x}}\phi^S$ and solve the Laplace equation to obtain $\partial\phi/\partial z$ when determining the time derivatives of η and ϕ^S. The HOS method is used to efficiently compute $\partial\phi/\partial z$ with a time complexity of $O(N\log N)$ and the fourth-order Runge–Kutta method is applied for the temporal integration of Eq. (5). A brief introduction to the numerical implementation of HOS is provided in §2.3.1. In this work, the customized GPU version of HOS-ocean developed by Lu et al. (2022) is employed to solve the far field potential domain.

2.2 Two-way coupling strategy

2.2.1 Flow field discretization

One can assume that the viscosity and nonlinearity primarily impact the flow region near the structure, while in the far-field region, the flow can be approximated as irrotational with non-breaking waves. This allows for the discretization approach shown in Figure 1.

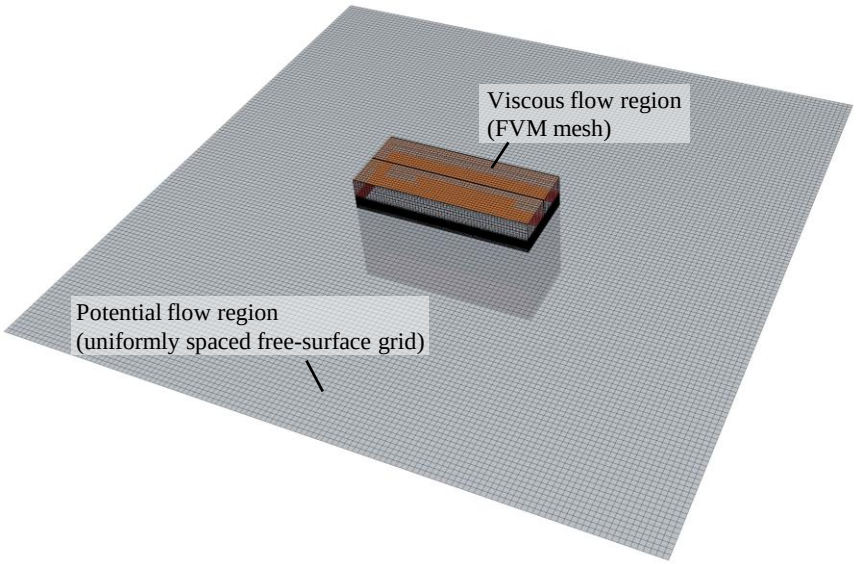

Figure 1: Schematic of the flow field discretization for two-way coupling method.

In the region surrounding the structure, termed the viscous flow region, discretization is carried out using the FVM with the N–S equations as governing equations. Outside this region, the water surface is discretized using a uniformly spaced grid, applying a pseudo-spectral method with the Laplace equation as the governing equation; this area is known as the potential flow region. Additionally, the uniformly spaced grid also cover the viscous flow region (including areas occupied by the structures). Together, the grids in both the viscous and potential flow regions form a complete pseudo-spectral collocation grid which is used for fast Fourier transform (FFT). This grid, called the spectral layer, records the free-surface wave elevation η_{HOS} and free-surface velocity potential ϕ_{HOS}^{S}.

Together, the spectral layer and the finite volume computational domain form an integrated computational domain. If the water velocity field is denoted by **U**, then **U** in the viscous flow region corresponds to the velocity field $\mathbf{U}_{\mathrm{OF}}$ within the volumetric grid, while in the potential flow region, **U** is represented by the velocity potential $\nabla\phi_{\mathrm{HOS}}$:

$$\mathbf{U} = \begin{cases} \mathbf{U}_{\mathrm{OF}} & \text{in the viscous flow region} \\ \nabla\phi_{\mathrm{HOS}} & \text{in the potential flow region} \end{cases} \tag{7}$$

where ϕ_{HOS} is the spatial velocity potential distribution determined by η_{HOS} and ϕ_{HOS}^{S}. It is noted that $\mathbf{U}_{\mathrm{OF}}$ does not necessarily equal to $\nabla\phi_{\mathrm{HOS}}$ in the potential flow region overlapping with the viscous flow region.

To enhance simulation accuracy and avoid convective terms due to reference frame movement, the potential flow is simulated in an earth-fixed coordinate system. For simulations involving moving structures, the viscous flow region moves freely within the earth-fixed spectral layer.

2.2.2 Potential-to-viscous coupling: velocity field transition via relaxation

In this two-way coupling approach, each time step begins by advancing the potential flow region. This is followed by advancing the viscous flow region. Using the free-surface elevation and velocity potential at time t_n, the free surface and velocity potential for the next time step are calculated directly via the fourth-order explicit Runge–Kutta scheme, producing the velocity field $\nabla\phi_{\mathrm{HOS}}$ at t_{n+1}. This

potential flow velocity field provides boundary conditions for the viscous flow region, enabling it to advance in time implicitly.

To ensure a smooth transition between the potential and viscous flow regions, the viscous flow velocity field undergoes a relaxation procedure after each time step. This procedure smoothly absorbs vorticity near the coupling boundary, maintaining coherence across regions. The relaxation procedure, modified from Choi et al. (2018), follows three key steps:

i. The entire velocity field of the spectral layer is calculated from the current free surface η_{HOS} and free-surface velocity potential ϕ^{S}_{HOS} using the H_2 operator (Bateman et al., 2003).

ii. B-spline interpolation is used to map the spectral layer's velocity field onto the viscous region's volumetric grid.

iii. The viscous flow field is then relaxed according to:

$$\xi_{\mathrm{relax}} = \mathcal{R}\xi_{\mathrm{HOS}} + (1-\mathcal{R})\xi_{\mathrm{OF}} \tag{8}$$

Here, ξ represents flow field parameters, such as velocity, volume fraction, etc; $\mathcal{R}$ is a relaxation function that smoothly transitions from 1 at the viscous region's coupling boundary to 0 over a defined distance. This function follows the exponential form used in Waves2Foam (Jacobsen et al., 2012). During the relaxation process, mass conservation is not explicitly enforced in the overlap region. As a result, mass conservation in the overlap (or transition) region can be considered as only being approximately achieved through the velocity potential correction. The rationale behind this approach is that, in the context of two-way coupled simulations, the viscous domain represents only a part of the overall flow field, and its boundaries are not rigid walls. As a result, both physically and numerically, the total mass in the viscous domain is not strictly constant and may temporarily increase or decrease. It is worth noting that, within our algorithm, errors due to small violations of mass conservation do not accumulate over time and do not cause instability. This is because the small free-surface variations (rise or fall) in the viscous domain, caused by these errors, are fed back to the potential-flow field in the form of correction terms, leading to compensatory fluxes at the viscous boundaries provided by the potential-flow solution, thereby maintaining overall system balance. To optimize the computational efficiency, GPUs are used for the potential flow calculations and interpolations (Lu et al., 2022).

This coupling method structurally looks similar to the one-way coupling approaches of Choi et al. (2018) and Zhuang and Wan (2021) but has a distinct functionality. The one-way coupling of Choi et al. (2018) relies on the relaxation step to absorb non-incident wave components within the relaxation zone. In contrast, the relaxation step in our proposed approach does not absorb non-incident wave components. Instead, it serves to provide accurate boundary conditions for each successive time step, while simultaneously absorbing vorticity near the boundary. This new approach enables the irrotational waves to pass from the viscous region into the spectral layer without interference.

2.2.3 Viscous-to-potential coupling: velocity potential correction based on free-surface velocity

The SCL method introduces a velocity potential correction approach that leverages the differences in vertical velocity at the free surface between the viscous and potential flow regions. This approach effectively transfers wave information from the viscous flow region to the potential flow region. A flowchart of the two-way coupling process is shown in Figure 2.

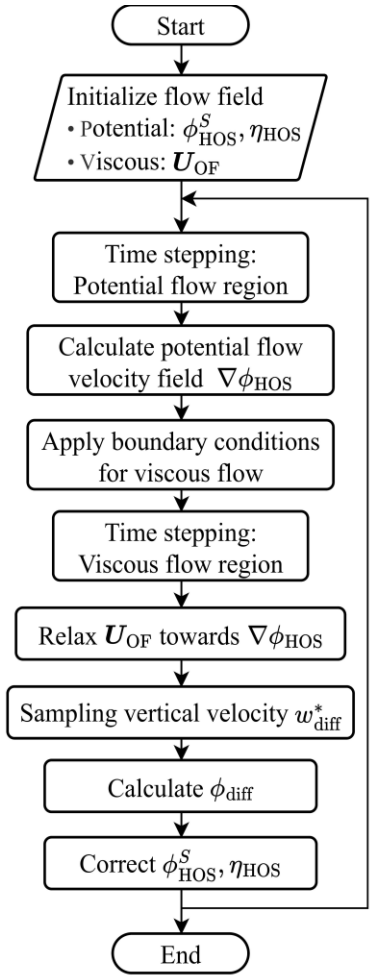

Figure 2: Schematic of two-way coupling.

At the start, the velocity flow field is initiated. According to Helmholtz's theory of velocity decomposition, the total velocity field in the viscous flow region can be expressed as the sum of irrotational and rotational parts:

$$\mathbf{U}_{\mathrm{OF}} = \mathbf{U}_p + \mathbf{U}_n = \nabla\phi_{\mathrm{OF}} + \mathbf{U}_n \tag{9}$$

Here, $\mathbf{U}_{\mathrm{OF}}$, $\mathbf{U}_p$, and $\mathbf{U}_n$ represent the total, irrotational, and rotational velocity fields, respectively, with ϕ_{OF} denoting the velocity potential for the irrotational component. This decomposition is not unique. In the ideal case where the viscous-flow and potential-flow solvers are perfectly coupled, ϕ_{HOS} equals ϕ_{OF}, and ϕ_{OF} minimizes $\|\mathbf{U}_n\|_2$. In practice, however, viscous effects and structural disturbances inevitably introduce discrepancies between these potentials as the fluid domain evolves. To mitigate this, we apply a free-surface-based correction at each time step to adjust ϕ_{HOS} toward ϕ_{OF}.

A hollow sampling zone near the free surface is established, defined by the single-valued plane $\eta^*(x, y)$ (see Figure 3) to sample the vertical velocity.

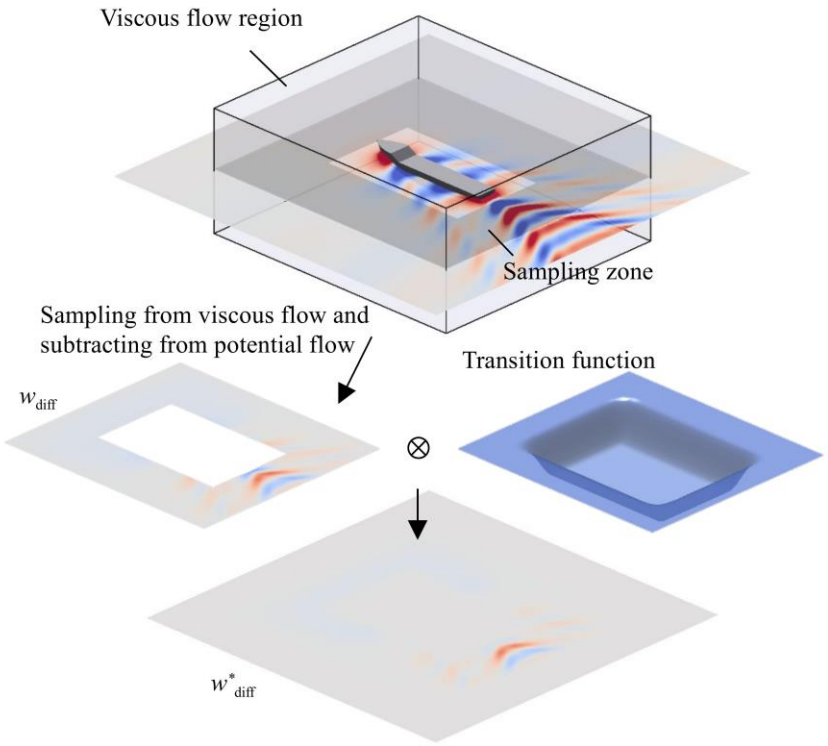

Figure 3: Sampling and calculation of correction velocity. w_{diff} is defined in Eq. (10) and w^*_{diff} defined in Eq. (11).

At the end of each time step, the vertical velocity difference between the viscous and potential flow fields is calculated as:

$$w_{\text{diff}} = \frac{\partial \phi_{\text{OF}}}{\partial z} - \frac{\partial \phi_{\text{HOS}}}{\partial z} \approx w_{\text{OF}} - \frac{\partial \phi_{\text{HOS}}}{\partial z} \quad \text{on } z = \eta^* \tag{10}$$

where w_{OF} represents the sampled vertical velocity in the viscous flow region, which approximates $\partial \phi_{\text{OF}} / \partial z$.

The relaxation operation discussed in §2.2.2 ensures that w_{diff} approaches zero smoothly at the interface between the viscous and potential flow regions. A transition function $\mathcal{T}(x, y)$ is introduced, which takes a value of 0 in the unsampled zone of the viscous flow region and gradually transitions to 1 within the sampling zone (see Figure 3). The fundamental rule for dividing the zones is that the sampling zone should contain only free-surface profiles consistent with potential flow theory, whereas all regions where the free surface may violate this assumption (e.g., extreme steep waves, breaking waves, etc.) must be placed entirely within the unsampled zone. A correction velocity for the potential flow velocity field, w^*_{diff}, comes from multiplying w_{diff} by $\mathcal{T}$:

$$w^*_{\text{diff}}(x, y) = \mathcal{T}(x, y) w_{\text{diff}}(x, y) \tag{11a}$$

$$\mathcal{T}(x, y) = 1 - \frac{1}{4}\left[\text{erf}\left(\frac{4d_x}{l_x} - 2\right) + 1\right]\left[\text{erf}\left(\frac{4d_y}{l_y} - 2\right) + 1\right] \tag{11b}$$

where d_x and d_y denote the shortest distances from an arbitrary point (x, y) within the viscous region to the nearest boundaries in the x- and y-directions, respectively; l_x and l_y are the characteristic widths of the sampling region inside the viscous region along the x- and y-directions, which control the spatial decay

scale of the sampling weight near the boundaries; erf is the error function. With this definition, when the distance from a point (x, y) to the boundary of the viscous region exceeds the corresponding characteristic width l_x and l_y in both direction, the value of $\mathcal{T}(x, y)$ can be regarded as 0, and the corresponding region is excluded from sampling.

Using w^*_{diff}, the correction velocity potential ϕ_{diff} is computed, which satisfies:

$$\frac{\partial \phi_{\text{diff}}}{\partial z} = w^*_{\text{diff}} \quad \text{on } z = \eta^* \tag{12}$$

ϕ_{diff} is defined within the same computational domain as the HOS layer. Eq. (12) provides the boundary condition within the viscous region. For locations outside the viscous region, the boundary condition on the free surface is given by $\partial\phi_{\text{diff}}/\partial z = 0$. A numerical algorithm for efficiently calculating ϕ_{diff} with a time complexity of $O(N\log N)$ is presented in §2.3.2.

The difference between the wave elevations in the potential and viscous flow regions is calculated as:

$$\eta_{\text{diff}} = \mathcal{T}(x, y)(\eta_{\text{OF}} - \eta_{\text{HOS}}) \tag{13}$$

At each time step, the flow field stored in the potential flow spectral layer is corrected based on the calculated difference:

$$\begin{aligned} \eta_{\text{HOS}}{}' &= \eta_{\text{HOS}} + \alpha\eta_{\text{diff}} \\ \phi_{\text{HOS}}{}' &= \phi_{\text{HOS}} + \alpha\phi_{\text{diff}} \end{aligned} \tag{14}$$

Here, α is a relaxation factor that enhances the stability of the numerical calculations. In this study, α is set to 0.05.

2.3 Numerical algorithm and implementation

2.3.1 HOS method

In this study, the HOS method is applied to simulate the potential flow. This pseudo-spectral approach efficiently computes the vertical velocity on a nonlinear free surface under Dirichlet boundary conditions, achieving a time complexity of $O(N\log N)$. To provide the basis for the velocity correction algorithm in §2.3.2, the HOS method is briefly presented. For further details on the derivation and implementation of the HOS method, readers can refer to the work of Dommermuth and Yue (1987).

Given η and ϕ^S in the spectral layer, the HOS method first expresses the velocity potential $\phi(x, y, z)$ as a sum of basis functions:

$$\phi(x, y, z) = \text{Re}\left(\sum_i A_i S_i(x, y, z)\right) \tag{15}$$

where A_i represents the complex amplitude and S_i are Fourier basis functions defined as:

$$S_i = \frac{\cosh\big(|\mathbf{k}_i|(z + d)\big)}{\cosh(|\mathbf{k}_i|d)} \exp\Big(\text{i}\big(k_{ix}x + k_{iy}y\big)\Big) \tag{16}$$

Here, k_{ix} and k_{iy} are wavenumbers, and $|\mathbf{k}_i| = \sqrt{k_{ix}^2 + k_{iy}^2}$ is the wavenumber magnitude. The basis functions S_i inherently satisfy the Laplace equation and the bottom boundary condition. Thus, solving for the velocity potential reduces to determining the coefficients A_i that satisfy the free-surface Dirichlet condition. To compute A_i efficiently, the HOS method perturbs the velocity potential into a series expansion by order:

$$\phi = \sum_{i=1}^{\infty} \phi^{(i)} = \phi^{(1)} + \phi^{(2)} + \phi^{(3)} + \cdots \tag{17}$$

Assuming a small wave steepness, a Taylor series expansion at $z = 0$ yields:

$$\begin{aligned} \phi^{(1)}(x,y,0) &= \phi^S \\ \phi^{(m)}(x,y,0) &= -\sum_{k=1}^{m-1} \frac{\eta^k}{k!} \frac{\partial^k}{\partial z^k} \left(\phi^{(m-k)}(x,y,0) \right), m > 1 \end{aligned} \tag{18}$$

The vertical velocity on the free surface is then given by:

$$\frac{\partial \phi}{\partial z} = \sum_{k=1}^{M} \left(\frac{\eta^{k-1}}{(k-1)!} \frac{\partial^k}{\partial z^k} \sum_{m=1}^{M-k+1} \phi^{(m)}(x,y,0) \right) \tag{19}$$

where M, the truncation order for the HOS expansion, is set to $M = 3$ in this study. Once $\partial\phi/\partial z$ has been calculated, the time-domain integration of the free-surface conditions, as in Eq. (2), is performed using a fourth-order Runge–Kutta scheme.

2.3.2 Computation of the correction velocity potential

It is essential to correct the velocity potential before coupling to maintain the numerical stability and accuracy. Using a method similar to the HOS approach, the correction velocity potential ϕ_{diff} is calculated by combining the pseudo-spectral method with a perturbation expansion. Given the known free surface $z = \eta$ and vertical velocity $\partial\phi/\partial z = w$, the Taylor expansion and perturbation expansion are applied on the plane $z = 0$, obtaining:

$$\begin{aligned} w(x,y,\eta) &= \frac{\partial}{\partial z}\phi(x,y,\eta) = \sum_{k=0}^{\infty} \frac{\eta^k}{k!} \frac{\partial^{k+1}}{\partial z^{k+1}} \phi(x,y,0) + \cdots \\ &= \frac{\partial}{\partial z}\phi^{(1)}(x,y,0) + \eta \frac{\partial^2}{\partial z^2}\phi^{(1)}(x,y,0) + \frac{\eta^2}{2}\frac{\partial^3}{\partial z^3}\phi^{(1)}(x,y,0) + \cdots \\ &+ \frac{\partial}{\partial z}\phi^{(2)}(x,y,0) + \eta \frac{\partial^2}{\partial z^2}\phi^{(2)}(x,y,0) + \cdots \\ &+ \frac{\partial}{\partial z}\phi^{(3)}(x,y,0) + \cdots \end{aligned} \tag{20}$$

The terms are then grouped by order, giving:

$$
\begin{aligned}
\frac{\partial}{\partial z}\phi^{(1)}(x,y,0) &= w(x,y,\eta) \\
\frac{\partial}{\partial z}\phi^{(2)}(x,y,0) &= -\eta\frac{\partial^2}{\partial z^2}\phi^{(1)}(x,y,0) \\
\frac{\partial}{\partial z}\phi^{(3)}(x,y,0) &= -\eta\frac{\partial^2}{\partial z^2}\phi^{(2)}(x,y,0) - \frac{\eta^2}{2}\frac{\partial^3}{\partial z^3}\phi^{(1)}(x,y,0) \\
\frac{\partial}{\partial z}\phi^{(m)}(x,y,0) &= -\sum_{k=1}^{m-1}\frac{\eta^k}{k!}\frac{\partial^{k+1}}{\partial z^{k+1}}\phi^{(m-k)}(x,y,0), \quad m>1
\end{aligned}
\tag{21}
$$

Referring to Eqs. (15) and (16), one can obtain:

$$
\begin{aligned}
\phi(x,y,0) &= \sum_i A_i \exp\left(\mathrm{i}\left(k_{ix}x + k_{iy}y\right)\right) \\
&= \mathcal{F}^{-1}(A)
\end{aligned}
\tag{22}
$$

where $\mathcal{F}^{-1}$ is the Inverse Fourier Transform. Similarly, the z-derivative of the velocity potential is:

$$
\frac{\partial}{\partial z}\phi(x,y,0) = \mathcal{F}^{-1}\left(A|\mathbf{k}|\tanh(|\mathbf{k}|d)\right) \tag{23}
$$

Upon solving for each order of the velocity potential on the $z = 0$ plane as outlined in Eq. (21), the complex amplitude A is efficiently calculated using FFT, providing the spatial distribution of the velocity potential. The computational overhead introduced at each time step is negligible. This is primarily because (i) the correction term is evaluated only once per step, without being involved in the Runge–Kutta sub-iterations, and (ii) its evaluation is further accelerated through GPU parallelization.

2.3.3 Sampling of vertical velocity in viscous flow region

In the proposed SCL method, accurate and efficient sampling of the vertical velocity field at the free surface within the viscous flow domain (denoted as w_{OF} in Eq. (10)) is crucial. This sampling affects the accuracy of the correction velocity potential ϕ_{diff} in Eq. (12). A minor error in ϕ_{diff} can be amplified by the sensitive HOS algorithm, propagating throughout the potential flow domain. Therefore, the efficiency of the sampling algorithm significantly impacts the overall computational overhead of the two-way coupling algorithm. The basic routines used in this work to perform the sampling are summarized as follows.

Step 1: *Re-construct the free surface employing the VOF field.*

The first challenge to be encountered lies in using the VOF method to capture the free surface in the viscous flow computation domain. In this method, the free surface is located at VOF = 0.5; however, its exact position needs to be determined using auxiliary techniques. This work makes use of OpenFOAM's *sampledIsoSurface* class to construct an isosurface ($VOF = 0.5$) in the viscous flow field, representing the free surface.

Step 2: *Interpolate the velocity field onto the free surface.*

Once the isosurface has been constructed, the viscous velocity field needs to be interpolated onto its vertices. This can be done via invoking the *sampledIsoSurface's* member function *sampleOnIsoSurfacePoints*.

Step 3: *Sample the elevation and vertical velocity from the free surface to HOS mesh nodes.*

Since the isosurface representing the free surface is constructed as an unstructured meshed surface, interpolated results from Step 2 are stored at the vertices of this surface. What remains challenging is the sampling of these results to the points of the HOS grid. This involves projecting a vertical line from the (x, y) coordinates of an HOS grid point along the z-axis, finding its intersection with the isosurface. The z coordinate and vertical component of the velocity at this intersection point are denoted as η_{OF} in Eq. (13) and w_{OF} in Eq. (10).

To achieve this, the *IntersectWithLine* function of the *cellLocator* object in the open-source Visualization Toolkit (VTK) library (Schroeder et al., 1998) is employed. This sampling method allows for the rapid and precise determination of the intersection points and the interpolation of the velocity field on these points. Moreover, the method can be significantly accelerated when performed on GPUs, which have already been used extensively to speed up the HOS solver and compute of relaxation zones in the presented coupled model. The sampling methods presented in this study can yield perfectly accurate interpolated data, provided that the computational domain is partitioned in strict accordance with the rules for defining sampling and non-sampling zones outlined in §2.2.3.

2.3.4 Mitigation of spurious velocity in viscous flow region

The limitations of the VOF algorithm can cause abrupt changes in fluid velocity field near the two-phase interface (the water surface), a phenomenon known as spurious velocity. This effect distorts the sampled w_{OF} values and introduce numerical errors in the two-way coupling. A common solution is to use the Ghost Fluid Method (GFM) (Peltonen et al., 2020), which reduce the spurious velocity near the free surface within the water phase. The GFM method however does not completely remove the surious velocities and while requires a sufficient grid density at the interface. To demonstrate the robustness of the two-way coupling algorithm developed in this study, we opted to use the original VOF. The sampling plane $\eta^*(x, y)$ is adjusted by positioning it slightly below the usual free surface $\eta_{(VOF=0.50)}$, thereby minimizing the influence of spurious velocities. The position of the new sampling surface is determined by Eq. (24), where the constant $\kappa = 2.0{\sim}4.0$ are recommended and 2.0 is used in rest of the paper (if not mentioned otherwise)

$$\eta^* = \eta_{(VOF=0.50)} - \kappa\left(\eta_{(VOF=0.50)} - \eta_{(VOF=0.99)}\right) \tag{24}$$

2.3.5 Wave generation and absorption

Since the SCL method integrates the viscous flow domains into a large computational potential flow domain, wave generation and absorption zones must be established at both ends of the potential flow domain. Incident waves are created in the potential flow region, travel into the viscous flow region, pass through it and re-enter the potential flow region. Ultimately, these waves dissipate in the wave absorption zone of the potential flow domain.

In the upstream wave generation zone, wave height and velocity potential on the free surface are relaxed at each time step using a ramp function:

$$\begin{aligned} \eta_{\mathrm{HOS}} &= \eta_{\mathrm{HOS}} + R(x)\left(\eta_{\mathrm{gen}} - \eta_{\mathrm{HOS}}\right) \\ \phi^S_{\mathrm{HOS}} &= \phi^S_{\mathrm{HOS}} + R(x)\left(\phi^S_{\mathrm{gen}} - \phi^S_{\mathrm{HOS}}\right) \end{aligned} \tag{25}$$

Here, η_{gen} and ϕ_{gen} represent the artificially defined wave height and velocity potential function, respectively. The ramp function $R(x)$ is defined as:

$$R(x) = \exp\left(-\left(\frac{3x - 3x_{\text{gen}}}{l_{\text{gen}}}\right)^8\right) \tag{26}$$

In this context, l_{gen} is the length of the wave generation zone and x_{gen} is the midpoint coordinate of this zone along the x-axis. In this study, the wave generation zone is established in the first one-eighth of the upstream potential flow domain.

In the downstream wave absorption zone, a Rayleigh damping term is introduced to the dynamic condition of the free surface to facilitate wave dissipation:

$$\frac{\partial \phi^S}{\partial t} = \frac{1 + |\nabla_{\mathbf{x}}\eta|^2}{2}\left(\frac{\partial \phi}{\partial z}\right)^2 - g\eta - \frac{|\nabla_{\mathbf{x}}\phi^S|^2}{2} - \nu\phi^S \tag{27}$$

where ν represents the Rayleigh damping coefficient, which increases quadratically within the wave absorption zone:

$$\nu(x) = \nu_0\left(\frac{x - x_{\text{damp}}}{l_{\text{damp}}}\right)^2 \tag{28}$$

Here, l_{damp} is the length of the wave absorption zone and x_{damp} is the starting coordinate of this zone. In this study, the last one-eighth of the downstream potential flow domain is designated as the wave absorption zone.

3 Validation and results analysis

3.1 2DV regular wave simulations

3.1.1 Simulation setup

The performance of SCL method is first evaluated in modeling pure-wave propagations. These benchmark cases are the key to verify the ability of the coupling scheme to retain the incident wave characteristics with very high accuracy and without introducing undesired disturbances that could alter the original dispersion relation. This verification serves as the cornerstone for accurately simulating more complex wave–structure interaction cases. The coupled simulation of 2DV nonlinear regular waves is first validated. The wave parameters used in this test are listed in Table 1. The stream-function-based open-source library CN-Stream (Ducrozet et al., 2019) is used to generate the nonlinear regular ocean waves in the HOS solver. The results are compared with the pure HOS solution (i.e. wave propagation in the same HOS domain without coupling with OF domain).

Table 1: Characteristics of simulated regular waves in 2DV cases.

Parameter (Unit)	Symbol	Value
Period (s)	T	6.0
Wavelength (m)	λ	56.4
Wave Height (m)	H	1.015

Parameter (Unit)	Symbol	Value
Water Depth (m)	h	∞
Wave Slope	$\varepsilon = kH/2$	0.05655
Wavenumber	$k = 2\pi/\lambda$	0.11143

The numerical domain is illustrated in Figure 4. In the sketch, L_{HOS} is the length of the potential domain Ω_{HOS}, L_{OF} is the total length of viscous domain Ω_{OF}, ω_L and ω_R are the lengths of the relaxation zones next to the inlet and outlet of Ω_{OF}, respectively. To ensure computational efficiency, the water depth H_{water} in Ω_{OF} does not need to match the actual water depth h in the potential domain Ω_{HOS}. An additional relaxation zone ω_B is added at the bottom of Ω_{OF} to minimize the effects of this mismatch. Another key configuration of this coupled simulation is the length of the sampling zone in Ω_{OF}. The vertical velocity at the free surface in this zone is sampled and passed to the HOS solver to calculate the correction velocity potential. In the presented 2DV simulations, ξ_L and ξ_R are the lengths of the sampling zones next to the inlet and outlet, respectively, and are determined by $\xi_{(L,R)} = 1.2\omega_{(L,R)}$. Waves are generated and damped by the wave making and absorbing zones, determined by σ and $\delta_{(L,R)}$, in the HOS field. The near field can be placed anywhere within the spectral layer but must be between the wave making zone on the left and the absorbing zone on the right. The near field is solved by the OpenFOAM(v2106) viscous solver *overWaveFoam*, which builds upon OpenFOAM's native overInterDyMFoam solver and incorporates additional functionalities such as numerical wave generation and absorption. The dotted red and the patterned orange regions indicate the HOS to OF (HOS→OF) relaxation zone and OF to HOS (OF→HOS) sampling zone respectively.

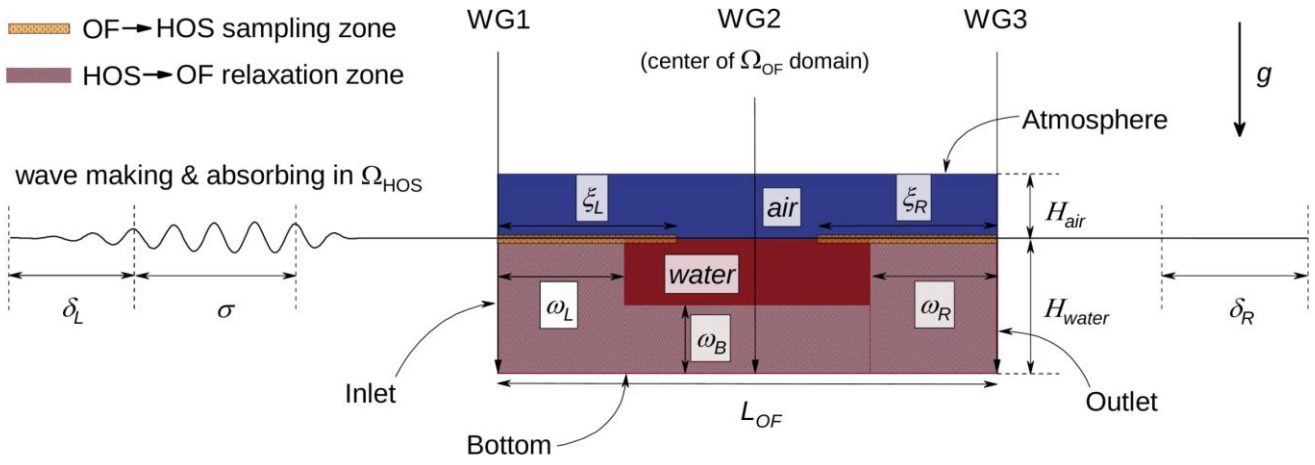

Figure 4: Sketch of 2D numerical domain used for the two-way simulations. The dotted red and patterned orange regions indicate the HOS-to-OF relaxation zone and OF-to-HOS sampling zone, respectively. The positions of wave sensors are indicated as WG1–WG3. Symbols $\xi_{(L,R)}$ are the lengths of the sampling zones, $\omega_{(L,R,B)}$ the lengths of the relaxation zones, $\delta_{(L,R)}$ the lengths of the wave absorbing zones, and σ the length of the wave making zone. g is the gravitational force.

The overall coupling procedure is explained further in Figure 5. Different overlapping regions are used depending on the coupling direction. The overlap regions employed for (i) HOS to CFD and (ii) CFD to

HOS are exemplified in Fig. 5(a) and (b), respectively. In Fig. 5(a), two relaxation zones, ω_L and ω_R, are defined upstream and downstream of the OpenFOAM computational domain. For each grid point located within these zones, a relaxation function $\mathcal{R}$ is assigned, taking values between 0 and 1 depending on its distance from the upstream or downstream boundary. During HOS-to-CFD coupling, the final velocity and surface elevation at any relaxation point are then evaluated using Eq. (8). In Fig. 5(b), we show how effective coupling nodes are defined within the part of the HOS domain overlapped by CFD, using ξ_L and ξ_R. For each effective node, the vertical velocity and elevation at the CFD free surface are sampled via vertical projection. An example of the coupling transition function $\mathcal{T}$ is also illustrated. Finally, Eqs. (10–14) are applied to correct and update the HOS variables.

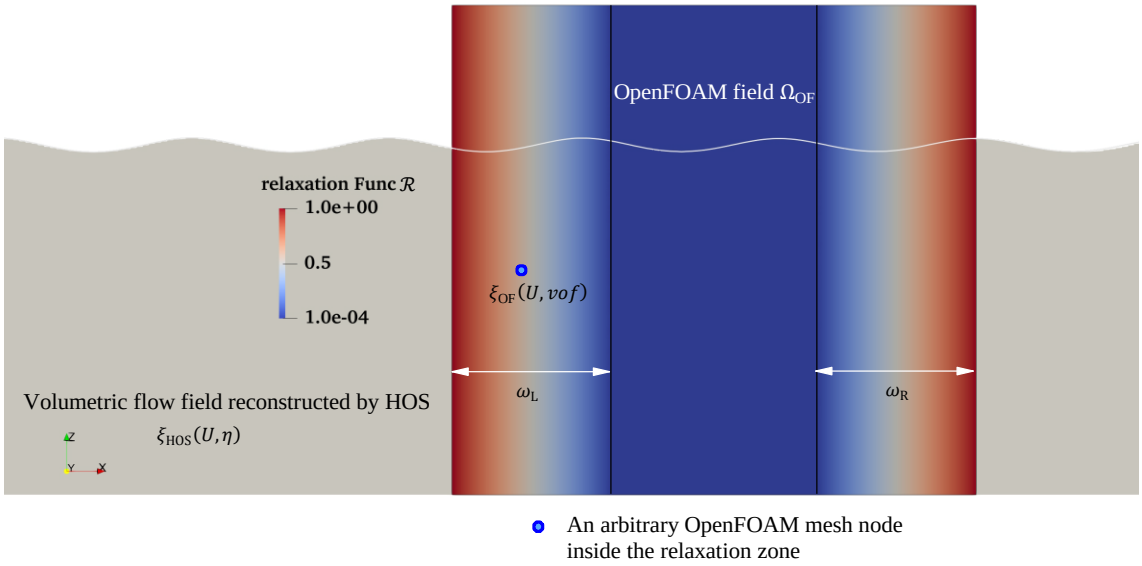

(a)

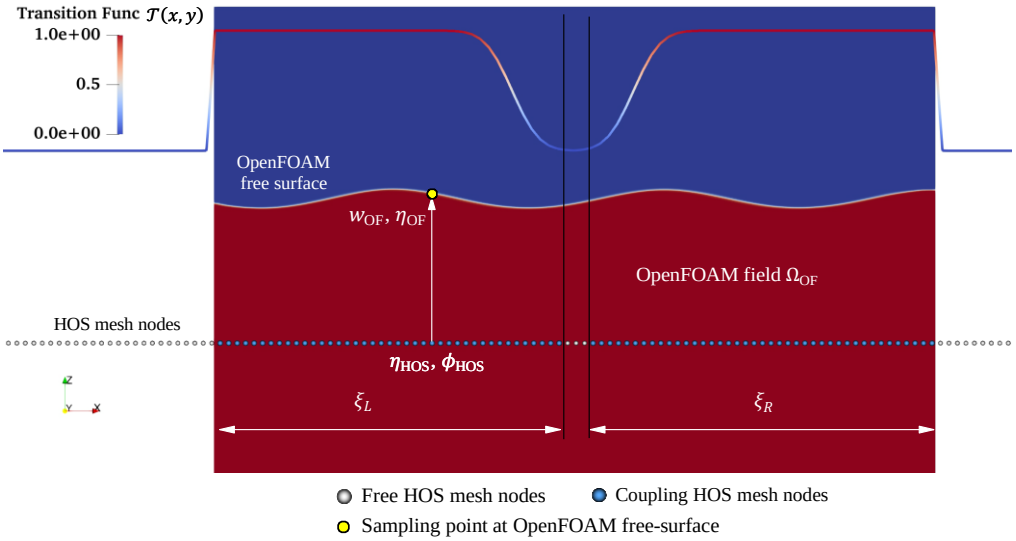

(b)

Figure 5: (a). HOS-to-CFD coupling using upstream and downstream relaxation zones ω_L and ω_R, with the relaxation function $\mathcal{R}$ applied to compute velocity and free-surface elevation (Eq. 8). (b). CFD-to-HOS coupling using effective overlap nodes inside ξ_L and ξ_R, where vertical projection is used to sample the velocity and free-surface elevation from CFD, combined with a transition function $\mathcal{T}$ to update HOS variables (Eqs. 10–14).

The boundary conditions used by the viscous near-field solver *overWaveFoam* for both the 2DV and 3D cases are presented in Table 2. The detailed configuration parameters used in the 2DV simulations are given in Table 3. Here, n_x and Δ_x are the number of discretized mesh and mesh size in the horizontal direction, respectively; Δ_z is the mesh size in the vertical direction and Δt is the time step; CFL and CFL_α are the Courant–Friedrichs–Lewy numbers for the viscous solver and the surface tracking. Using these parameters, simulations were performed on the medium mesh (Mesh #2). The correction surface velocity potential ϕ_{diff} was calculated from the vertical velocity $w_{(VOF=0.5)}$, as sampled from the OF velocity field at the isosurface on which $VOF = 0.5$, denoted as $\eta_{(VOF=0.5)}$.

Table 2: Numerical boundary conditions used by overWaveFoam.

Physical Boundaries	**p_rgh**	**U**	**alpha.water**
Inlet	zeroGradient	zeroGradient	zeroGradient
Outlet	zeroGradient	zeroGradient	zeroGradient
Atmosphere	totalPressure	pressureInletOutletVelocity	inletOutlet
Bottom	zeroGradient	zeroGradient	zeroGradient
Sides	empty(2D) / zeroGradient(3D)	empty(2D) / zeroGradient(3D)	zeroGradient
Hull	fixedFluxPressure	movingWallVelocity	zeroGradient

Table 3: Configuration parameters for coupled 2DV pure-wave simulations.

HOS		**overWaveFoam**			
n_x	1024	ω_L	1.0λ	Mesh #1 (coarse) $\Delta t \approx \frac{T}{100}$	$\Delta x = \lambda/40$
n_y	-	ω_R	1.0λ		$\Delta y(-)$
Δx	$\lambda/32$	ω_B	0.25λ		$\Delta z = H/10$
Δy	-	ξ_L	1.2λ	Mesh #2 (medium) $\Delta t \approx \frac{T}{200}$	$\Delta x = \lambda/80$
M	3	ξ_R	1.2λ		$\Delta y(-)$
L_{HOS}	32.0λ	H_{air}	$10.0H$		$\Delta z = H/25$
		H_{water}	$25.0H$	Mesh #3 (fine) $\Delta t \approx \frac{T}{300}$	$\Delta x = \lambda/120$
		CFL/CFL_α	$0.5/0.5$		$\Delta y(-)$
		L_{OF}	3.0λ		$\Delta z = H/40$

3.1.2 Identify sampling surface position to mitigate spurious velocity

The free surface comparison between two-way coupled 2DV and the non-coupled HOS simulations is shown in Figure 6. In this two-way coupled simulation, the correction velocity potential ϕ_{diff} was computed from $w_{VOF=0.5}$, i.e. without applying the sampling correction (-noShift). It is evident from Figure 6 that the computational results using two-way coupling with $w_{VOF=0.5}$ are not good. One can see the deviation in the surface elevation at WG1 and intensified when wave propagate toward WG3. The wave phase was significantly delayed at WG3. It is well known that viscous solver could alters the characteristics of the incident waves. However, the deviation at WG1 and significant deviation at WG3 are undesirable and could be artributed to numerical errors.

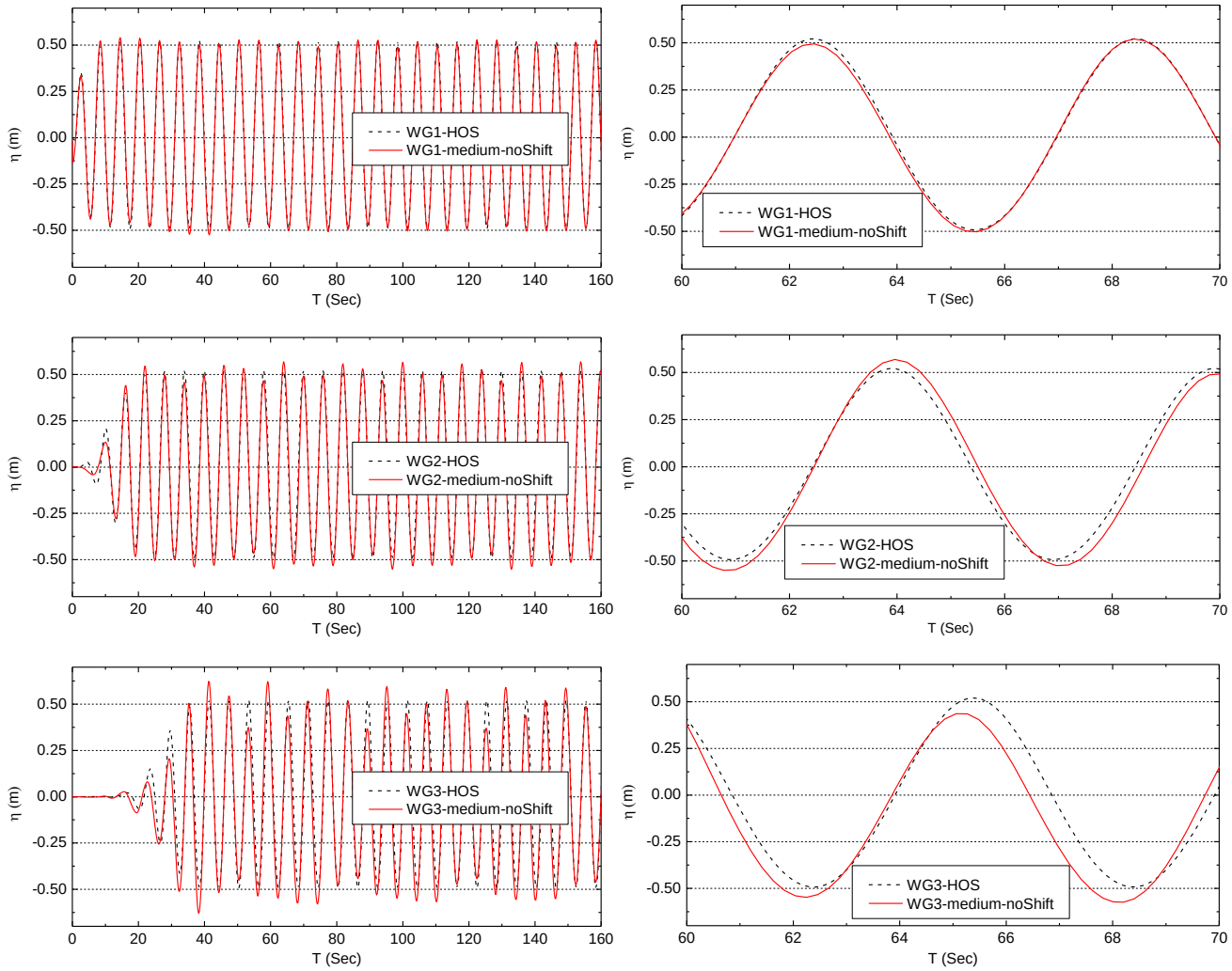

Figure 6: Comparison of free surfaces given by two-way coupled 2DV regular wave simulation and pure HOS simulation results. (a) Time history of η at WG1–WG3 from t=0–160 s (top to bottom); (b) zoomed-in time histories at WG1–WG3. The term "noShift" indicates that the coupling was performed without applying the sampling correction.

To understand what are the possible numerical errors, it is necessary to acknowledge that *overWaveFoam* uses the inherently diffusive VOF method to capture the free surface and employs a two-phase mixture approach, rather than applying an accurate two-fluid method to handle the air–water interface. Combined with the significant density difference between water and air, this leads to occasional non-physical disturbances in the velocity field near the free surface, commonly referred to as spurious velocities (Peltonen et al., 2020; Di Paolo et al., 2021; Landesman et al., 2024). This problem is clearly visualized in Figure 7. The coloured contour of velocity field near the isosurface commonly used to define the free surface, $\eta_{VOF=0.5}$, in Figure 7a show a thin region of unphysically high velocity magnitude, while a much more smoothed velocity region is seen at a certain distance below the free surface, e.g. at $\eta_{VOF=0.99}$. Further investigation on the vertical velocity U_z distribution along a vertical line in the OF domain in Figure 7b shows an unphysical oscillation in the velocity values appears near the free surface. A zoomed-in view of the vertical velocity around the oscillation in Figure 7c suggests a new shifted sampling location along the isosurface η^* to avoid the spurious velocity.

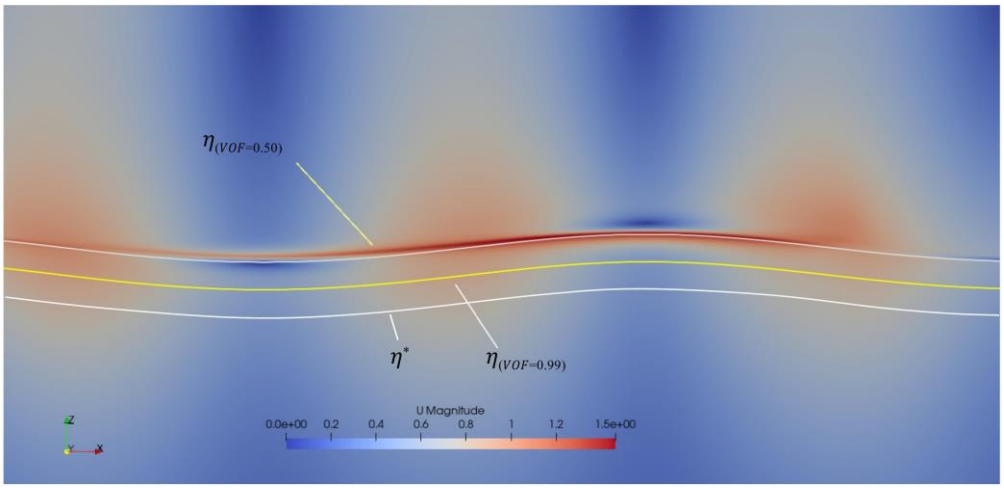

(a)

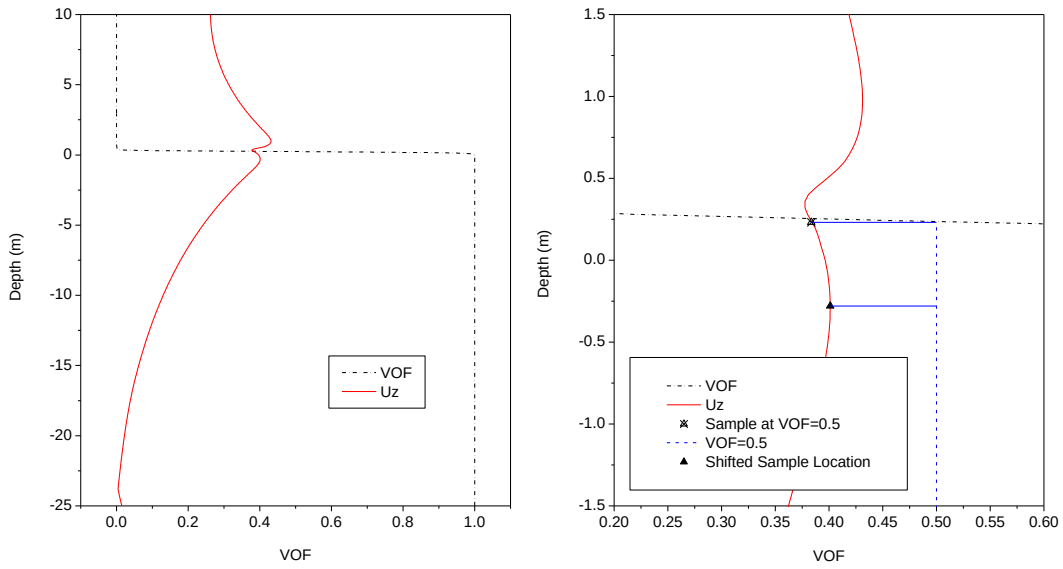

(b) (c)

Figure 7: Illustration of correction to the sampling of vertical velocity near the free surface solved by overWaveFoam. (a) coloured contour of velocity field near the free surface (VOF=0.5); (b) vertical velocity U_z distribution along a vertical line in the OF domain; (c) zoomed-in view of the vertical velocity U_z in vicinity of the free surface.

As discussed above, it is suggested that instead of directly using the sampled values at $\eta_{(VOF=0.5)}$ for the w_{OF} in Eq. 10, the velocity values w^* are sampled at a down-shifted location η^* and used to compute the correction free-surface vertical velocity w_{diff}. The down-shifted location is determined by Eq. (28). With this correction, the simulations were conducted again on the three meshes listed in Table 3. As shown in Figure 8, there is excellent agreement on mesh #3 (fine) at all three WGs after the proposed correction. The agreements at WG1 and WG2 on mesh #2 (medium) are also satisfactory, with only a slight underestimation observed at WG3. The underestimation of wave amplitude is more pronounced on mesh #1 (coarse) at WG2 and WG3 which could be attributed to the viscous effect.

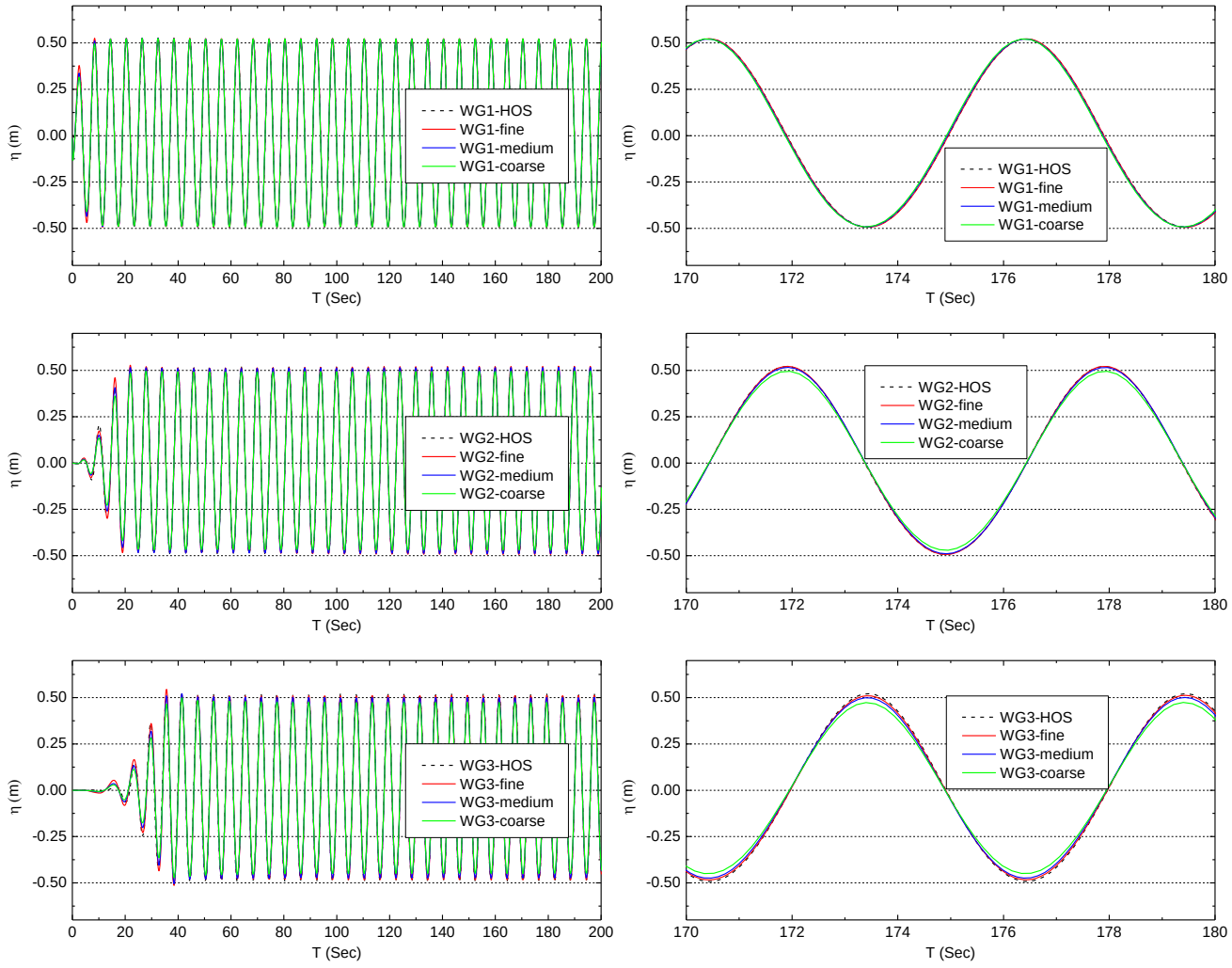

(a) (b)

Figure 8: Comparison of free surfaces given by two-way coupled 2DV regular wave simulation and pure HOS simulation results. Correction velocity potential ϕ_{diff} was computed from w_{diff}. (a) Time history of η at WG1–WG3 from t=0–200 s (top to bottom); (b) zoomed-in time histories at WG1–WG3.

The comparison of root mean squared error (RMSE) of surface elevation before and after shifting the sampling location at the three wave gauges is tabulated in Table 4.

Table 4: The root mean squared error (RMSE) of surface elevation before and after applying the shifted sampling.

RMSE of Surface Elevation	2-way coupling mesh #2 WG1	2-way coupling mesh #2 WG2	2-way coupling mesh #2 WG3
sampling at η^*	0.009862	0.006315	0.016500
sampling at $\eta_{VOF=0.50}$	0.015740	0.039530	0.105338

3.1.3 Vertical velocity distribution

Accurately predicting the characteristics of wave kinematics is the foundational prerequisite for further simulations of wave-structure interactions. Hence, the wave kinematics distribution along a vertical line at the location of WG2-3 during a whole cycle of the 15th wave period is also investigated. This period was selected because it is located approximately in the middle of the numerical time window, after the initial transient effects have diminished and before any potential long-time accumulation effects become significant. The wave field at this stage is therefore considered representative.

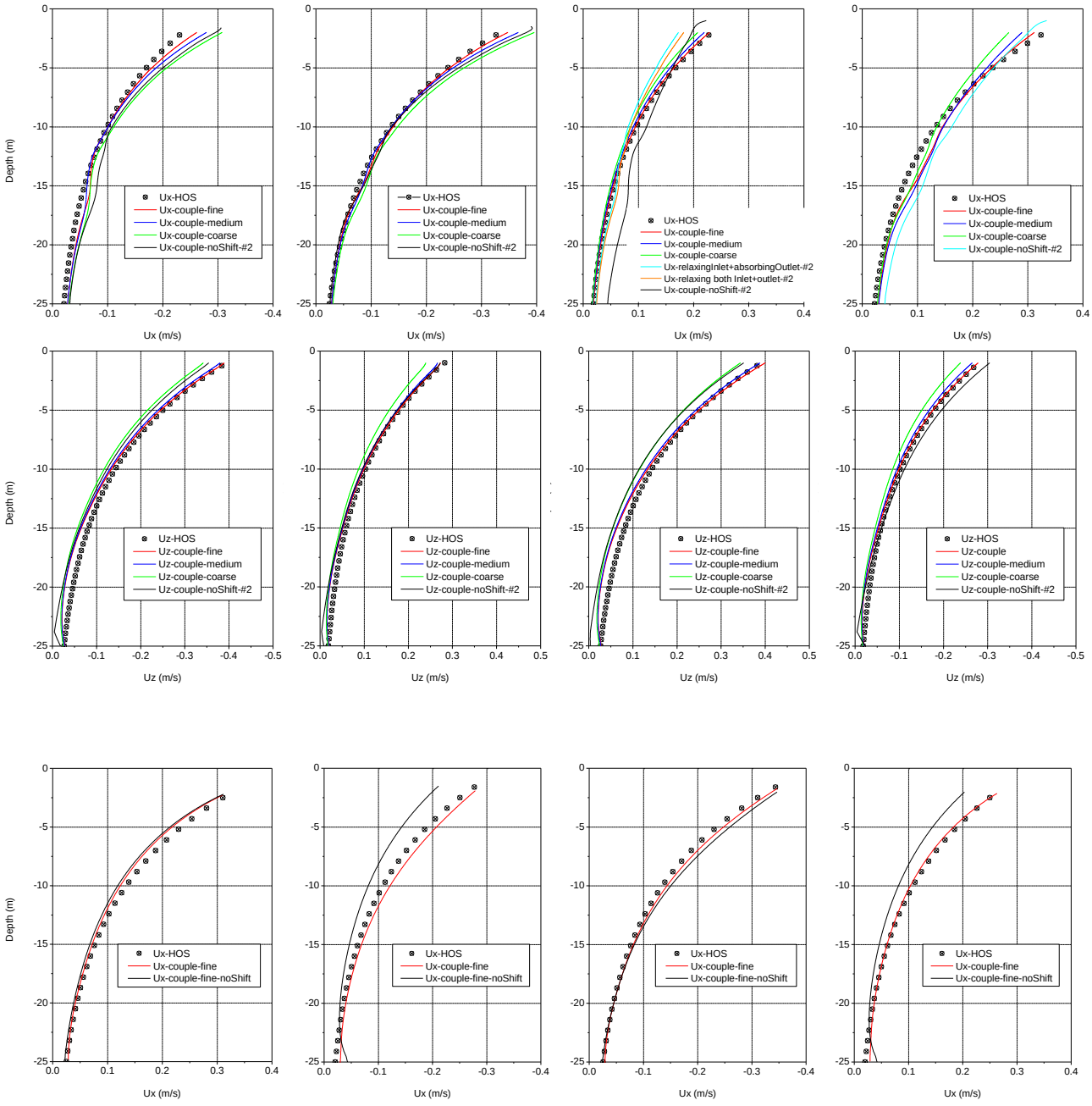

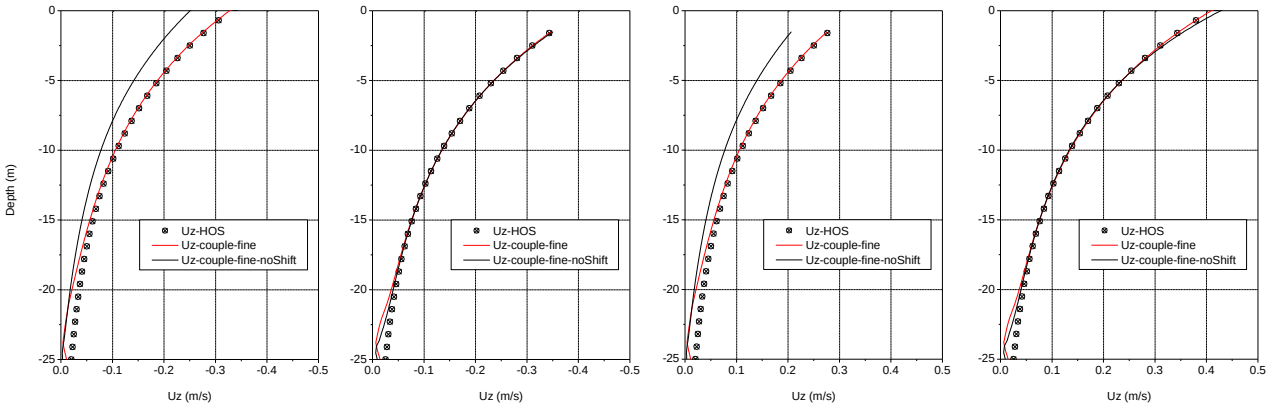

Figure 9: Comparison of depth distribution of horizontal (top panel) and vertical (bottom panel) velocities along the vertical line at (a) WG2 and (b) WG3 between 2DV coupled regular wave simulation and pure HOS solution during a complete cycle of the 15th wave period (t=90, 91.5, 93 and 94.5 second from left to right on each row).

As shown in Figure 9, the velocity field predictions obtained using the SCL coupling method (with adjusted sampling location) on the three test meshes align with the free surface comparison results in Figure 8 when compared to the pure HOS solution. The results on the fine mesh (mesh #3) are most consistent with the HOS solution, while the medium mesh (mesh #2) shows slightly less agreement but remains acceptable. The results on the coarse mesh (mesh #1) exhibit larger errors probably due to the mesh resolution being insufficient. Additionally, the comparison also shows the results on the medium mesh without applying the sampling correction (-noShift-#2). It is evident that the sampling correction significantly improves the computational results.

Furthermore, results for U_x at the 3rd time instant on the medium mesh using one-way coupling are also presented for comparisons. For the one-way coupling, the two most common approaches, which generally perform well when the viscous domain is relatively large, are used: (i) using HOS relaxation zone at inlet but absorb the waves at outlet by damping the field to calm state (-relaxingInlet-absorbingOutlet-#2), and (ii) using HOS relaxation zones at both the inlet and outlet (-relaxing-both-inlet-outlet-#2). Given the compact domain in our tests, the one-way coupling method failed to produce satisfactory results. The one-way coupling simulations overestimate the velocity at the bottom part of the water column while significantly underestimate the velocity near the free surface. The root mean squared errors (RMSE) of the computed U_x at the 3rd time instant are presented in Table 5, clearly highlighting the accuracy of various simulation approaches.

Table 5: The root mean squared error (RMSE) of U_x at the 3rd time instant for WG2 using both 1-way and 2-way coupling strategies. The value computed by HOS is employed as baseline solution. η^* and $\eta_{VOF=0.50}$ are defined in Eq. (24).

2-way coupling mesh #3 sampling at η^*	2-way coupling mesh #2 sampling at η^*	2-way coupling mesh #1 sampling at η^*	2-way coupling mesh #2 sampling at $\eta_{VOF=0.50}$	1-way coupling mesh #2 L: relax; R: absorb	1-way coupling mesh #2 L: relax; R: relax
0.00248	0.005876	0.0174	0.0659	0.0276	0.0323

To conclude, after a combined consideration of accuracy and efficiency, the SCL with adjusted sampling location on the medium mesh (#2) is adopted in all our wave simulations hereafter. The same mesh resolution is also recommended to the 3D scenarios.

3.1.4 Influence of relaxation length

The lengths of HOS→OF relaxation zone $\omega_{(L,R)}$ and of OF→HOS sampling zone $\xi_{(L,R)}$ is a very important pair of parameters in the SCL coupling method. To study the sensitivity of the choices of these parameters to the accuracy of results, simulations using different zone lengths are conducted. Four different HOS→OF relaxation zone lengths are tested, including $\omega_{(L,R)} = 1.2\lambda, 1.0\lambda, 0.6\lambda$ and 0.4λ . The OF→HOS sampling zone length are determined by $\zeta_{(L,R)} = 1.2\omega_{(L,R)}$. The time history of simulated η at WG1-WG3 for t=[170, 180] seconds are presented from top to bottom of Figure 10. It can be seen that the simulation accuracy improve when the relaxation length increases and the lengths of 1.2λ and 1.0λ

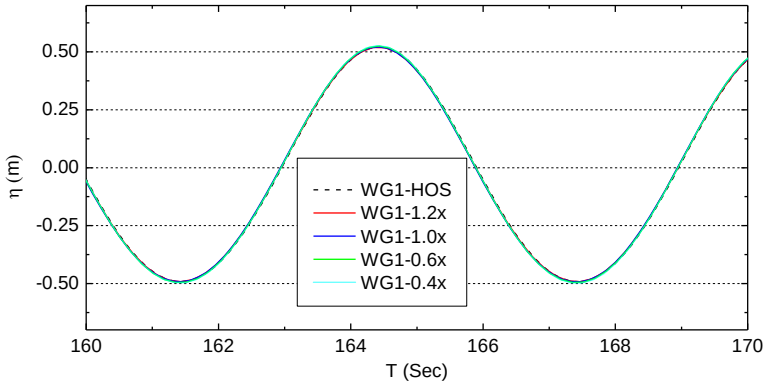

results in almost the same results. Thus, $\omega = 1.0\lambda$ is recommended for practical applications, as it provides the best balance between accuracy and computational cost.

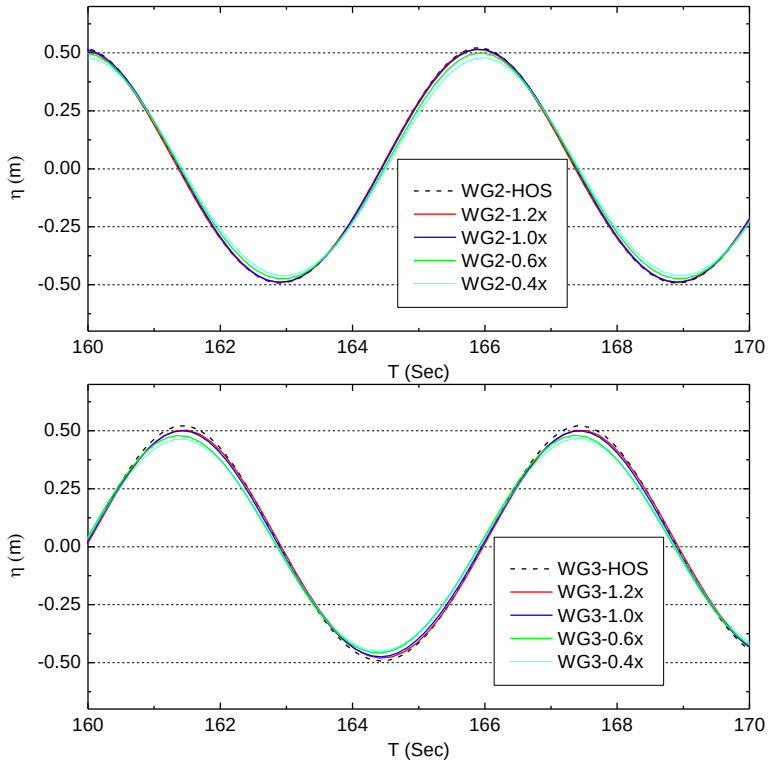

Figure 10: Sensitivity study of surface elevation with respect to the lengths of the sampling and relaxation zones in two-way coupled 2DV regular wave simulations.

3.2 3D regular wave simulations

In the previous sections, the model's performance in 2D pure-wave simulation scenarios was validated. The performance is now examined under the more demanding case of 3D wave simulations. It is well-known that the VOF-based viscous free surface solver suffers from a high level of numerical dissipation. Thus, it should not be applied to excessively large computational domains to prevent numerical errors from reducing the wave amplitude. On the other hand, overly compact computational domains can lead to other issues, such as boundary effects or non-physical reflections when the boundaries cannot absorb waves generated by wave–structure interactions within the domains. This contradiction will be shown effectively resolved within the present SCL two-way coupling framework.

The numerical domain is sketched in Figure 11. The area between the green dash-dot-lined box and the black solid-lined box is the OF→HOS relaxation zone, the area between the red dash-lined box and the black solid-lined box is the HOS→OF relaxation zone. It is noted that a pair zones of performing HOS→OF relaxation and OF→HOS sampling is also equipped at the top and bottom sides of the viscous domain, similar to the 2D cases. The parameters for the regular waves are listed in Table 6. Most of model parameters are directly taken from the 2DV cases, and those specific to 3D scenarios are defined in Table 7. The new parameters define the grid resolution and domain length in the additional spatial direction (y-direction) for both the HOS and *overWaveFoam* solvers. Free surface results of two-way coupled simulation are compared with the pure HOS and one-way coupling simulations.

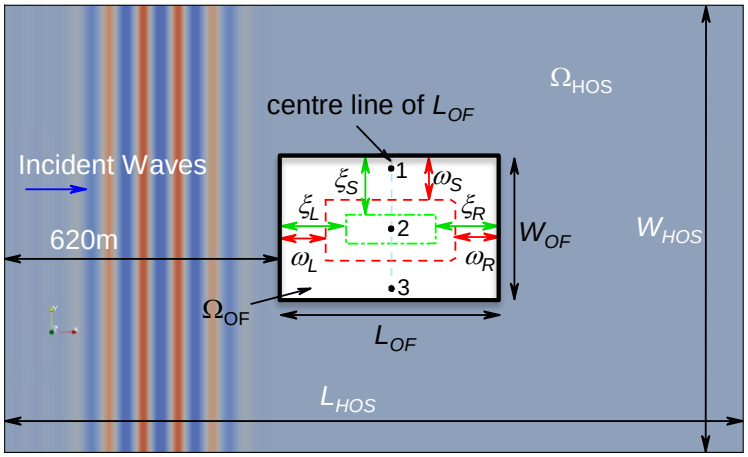

Figure 11: Schematics of the computational domain for 3D pure-wave simulations (top view, picture not to scale). The locations wave sensors WG1–WG3 are indicated. The meanings of the symbols are given in Figure 4.

Table 6: Characteristics of simulated regular waves in 3D cases.

Parameter and Unit	Symbol	Value
Period (s)	T	5.7
Wavelength (m)	λ	51.0
Wave Height (m)	H	1.4
Water Depth (m)	h	∞
Wave Slope	$\varepsilon = kH/2$	0.08624
Wavenumber	k	0.1232

Table 7: Model parameters specific to 3D pure-wave simulations (other parameters are the same as in Table 3). W_{HOS} and W_{OF} are the width of Ω_{HOS} and Ω_{OF} respectively

HOS		**overWaveFoam**			
n_y	640	ω_S	0.5λ	Mesh #2 (medium)	$\Delta x = \lambda/80$
Δy	$\lambda/32$	ξ_S	0.6λ		$\Delta y = \lambda/80$
W_{HOS}	20.0λ	W_{OF}	2.0λ		$\Delta z = H/25$

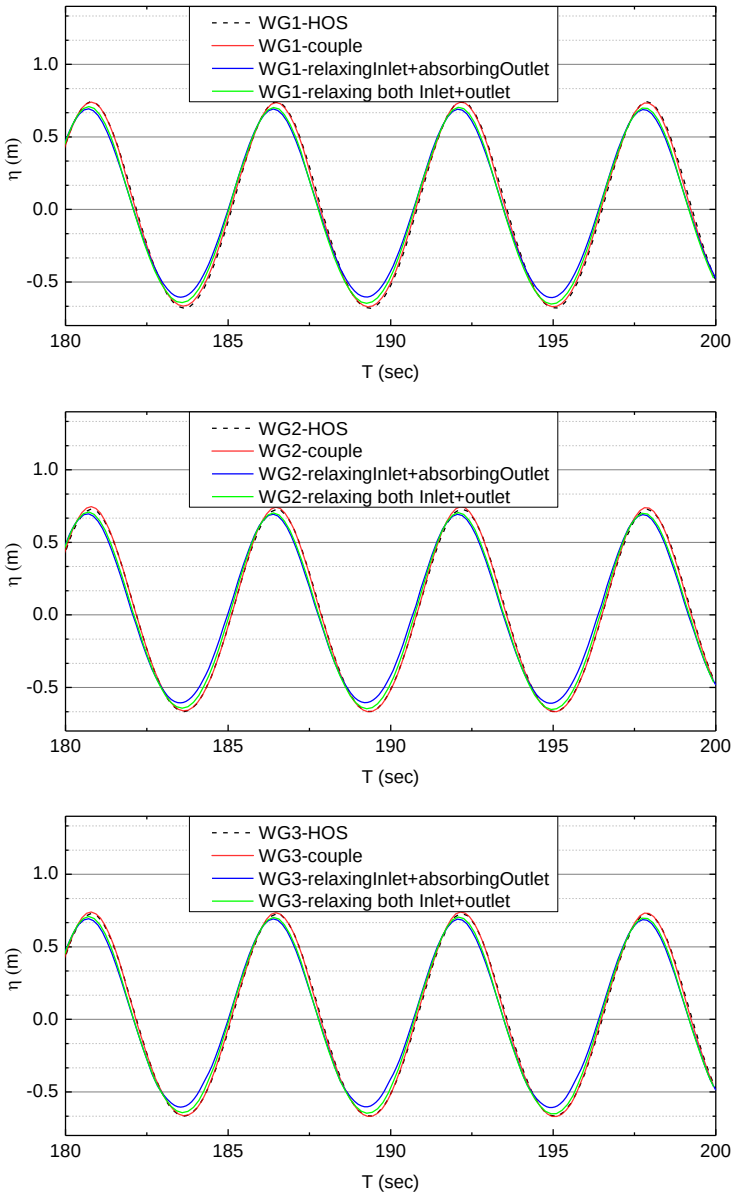

Figure 12: Comparison of free surfaces given by two-way coupled 3D regular wave simulation, pure HOS simulation, and one-way coupling (with "-relaxing-") results. From top to bottom: time histories of η from t=180–200 s at WG1–WG3.

Figure 12 presents comparisons of surface wave time series at WG1-3. One can observe that the two-way coupling model reproduces the incident regular waves better than the one-way coupling counterparts, in terms of maintaining both the phases and waves magnitude, under the same CFD viscous computational domain size. The two-way coupled model produced almost identical result to that of the pure HOS model. Slight phase shift and amplitude reduction are observed in the result of the one-way coupling with both relaxation at inlet and outlet. The one-way coupling with absorption at outlet performs the worst which could be artributed to the larger wave reflection at the outlet. Compared with 2D simulations, 3D computations indeed introduce additional challenges. The first is the significant increase in computational time, although, relative to single-domain non-coupled simulations, our coupled approach already achieves a substantial reduction. Another challenge lies in the careful design of mesh resolution in the horizontal plane. For long-crested waves, a denser grid is required along the primary wave-propagation direction (x), while the transverse direction (y) can be relatively coarser (by a factor of 2–3). In contrast, for short-

crested waves, it is preferable to use comparable mesh resolution in both the x and y directions. This is because the short-crested waves exhibit directional spreading, which leads to non-uniform distributions of wave elevation and phase speed in the transverse (y) direction. As a result, transverse gradients become more pronounced than in long-crested wave conditions.

Furthermore, the design of the HOS–CFD coupling region requires particular care in order to achieve the best performance.

3.3 Coupled wave pattern prediction for KCS sailing in calm water

In this section, the two-way coupling model will be applied to a more challenging test case: simulating the wave generation of a ship hull sailing in calm water using a compact viscous near-field region. The ship model used is the KRISO container ship KCS (Kim et al., 2001). In the study by Kim et al. (2001), extensive towing tank tests were conducted for the ship hull, providing a large amount of data including wave patterns and nominal wakes at several cross-planes near the stern. To date, this is the most widely used benchmark case for numerical predictions of hull-generated wave patterns (Larsson et al., 2013). The Froude number for this container ship is 0.26, resulting in approximately two fundamental wavelengths along the hull. In the published literature, this problem is typically addressed using traditional single-domain methods with very large computational domains, often exceeding six times the ship's length (Ozdemir et al., 2016). The ITTC procedure recommends that the inlet boundary should be 1-2 L_{pp}, where L_{pp} is the ship length, and the outlet boundary should be 3-5 L_{pp} away from the hull to avoid wave reflections (International Towing Tank Conference (ITTC), 2011). With the aid of two-way coupling, this problem is solved using a compact near-field computational domain of $2.3L_{pp}$ from the inlet to the outlet.

The design of the Ω_{OF} domain is illustrated in Figure 13. Similar to the definition in Figure 11, the area between the green dash-dot-lined box and the black solid-lined box is the OF→HOS relaxation zone, the area between the red dash-lined box and the black solid-lined box is the OF→HOS relaxation zone. The specific model parameters for this case are given in Table 8, where W_{HOS} and W_{OF} are the width of Ω_{HOS} and Ω_{OF}, respectively. Of the hull's six degrees-of-freedom, only heave and pitch were enabled in these simulations. The stabilized RANS model developed by Larsen and Fuhrman (2018) was employed to solve the turbulence effects in the Ω_{OF} domain. To model the hull sailing, OF domain containing the hull is sailed within the HOS domain at the hull's speed. It will be shown that using such a compact configuration, the proposed model can still predict the wave patterns surrounding the hull as well as those in the far-wake region accurately.

Table 8: Model parameters for KCS wave pattern prediction simulations using the two-way coupling method.

HOS		**overWaveFoam**			
n_x	1024	ω_L	$0.35L_{pp}$	Mesh #1 (coarse)	$\Delta x = L_{pp}/50$
n_y	512	ω_R	$0.35L_{pp}$		$\Delta y = L_{pp}/50$
Δx	$L_{pp}/64$	ω_B	$0.05L_{pp}$		$\Delta z = 0.0018L_{pp}$
Δy	$L_{pp}/64$	ξ_L	$0.455L_{pp}$	Mesh #2 (medium)	$\Delta x = L_{pp}/80$
M	3	ξ_R	$0.525L_{pp}$		$\Delta y = L_{pp}/80$
L_{HOS}	$16L_{pp}$	H_{air}	$0.175L_{pp}$		$\Delta z = 0.0011L_{pp}$

HOS		overWaveFoam			
W_{HOS}	$8L_{pp}$	H_{water}	$0.175L_{pp}$	Mesh #3 (fine)	$\Delta x = L_{pp}/120$
		L_{OF}	$2.3L_{pp}$		$\Delta y = L_{pp}/120$
		W_{OF}	$1.7L_{pp}$		$\Delta z = 0.0005L_{pp}$

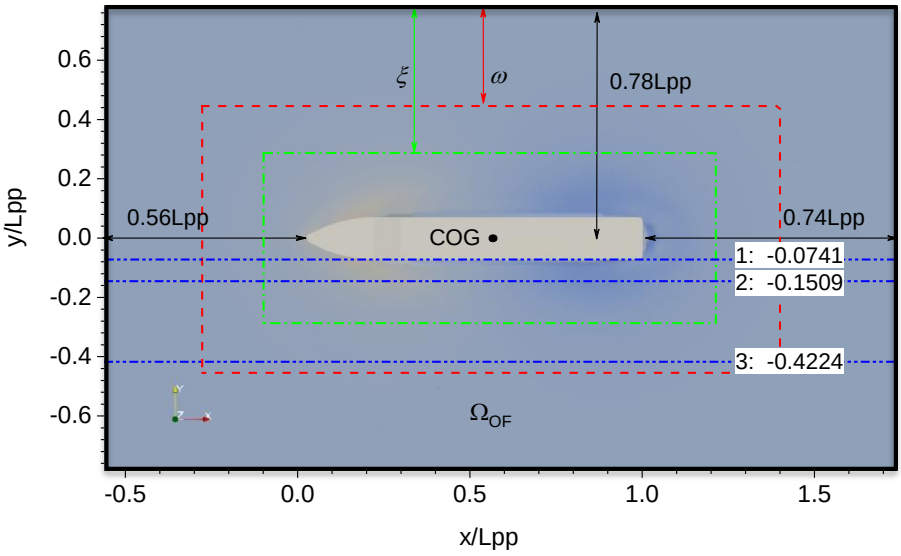

Figure 13: Schematics of the viscous domain for the numerical prediction of wave pattern produced by KCS sailing. The locations of three x-z cut-planes are indicated as blue dash-dot lines. COG refers to Center of Gravity.

Table 9: Computation times per time step for the viscous and potential-flow solvers

Module	Description	Time (s)	Fraction (%)
Potential flow solver	Pure HOS computation	0.27	2.8
Viscous flow solver	Pure OpenFOAM computation	7.01	73.6
Coupling module	Correction velocity potential computation	0.08	0.8
	HOS flow kinematic reconstruction	2.00	21.0
	OpenFOAM viscous flow sampling	0.16	1.7
Total		9.52	100

The computations were performed on a PC with an Intel Xeon 6330 CPU and an NVIDIA GeForce RTX 3080 GPU, using 48 CPU cores in parallel via OpenMPI. Taking a CFD mesh with grid resolution similar to Mesh #2 as an example, the typical computation times per time step for the viscous solver and the potential-flow solver are summarized in Table 9.

As shown in Table 9, the viscous computation requires approximately 7 s per time step, whereas the HOS computation only takes 0.27 s, which is negligible compared with the viscous calculation. The main computational cost in the coupling procedure is associated with the flow kinematic reconstruction, which still requires around 2 s even with GPU acceleration (Lu et al., 2022) and may be further optimized in the future. Overall, introducing potential-flow coupling results in a total time step computation that remains

significantly lower than the pure viscous solver. By increasing the computational time by only about 30%, the computational domain can be extended from 2.3 L_{pp} × 1.7 L_{pp} to 16 L_{pp} × 8 L_{pp}, corresponding to an approximately 32-fold increase in area.

The predicted wave pattern in the combined domain, Ω_{OF}+Ω_{HOS}, on the medium mesh is presented in Figure 14. It can be seen from Figure 14a that the wave generated by the KCS in calm water is well transmitted from the near field to the far field by the coupling algorithm. In Figure 14b and Figure 14c, the comparisons of the present results with the measurement by Kim et al. (2001) and the numerical result by Ozdemir et al. (2016) are shown. The two most pronounced wave systems at the bow and stern of the hull, as well as the systems originating with wave troughs at and after the two shoulders, are well predicted. No discontinuities of wave contours across the boundaries of viscous domain (indicated as the white box in all plots) are seen. It must be noted that, Ozdemir et al. (2016) used a much larger viscous domain in order to achieve this result. Furthermore, by using a background HOS domain simulations of a ship sailing over a long distance (in this case it is $16L_{pp}$) and a large ship wake could be realized with low overhead cost. As one can see in Figure 14a, due to the extremely low numerical dissipation characteristic of the HOS method, the generated waves evolve and propagate well in the far field until they reach the wave-absorbing zones surrounding the Ω_{HOS} and are absorbed. In constrast, a similar simulation in a single viscous domain could only modelled by special boundary condition treatments.

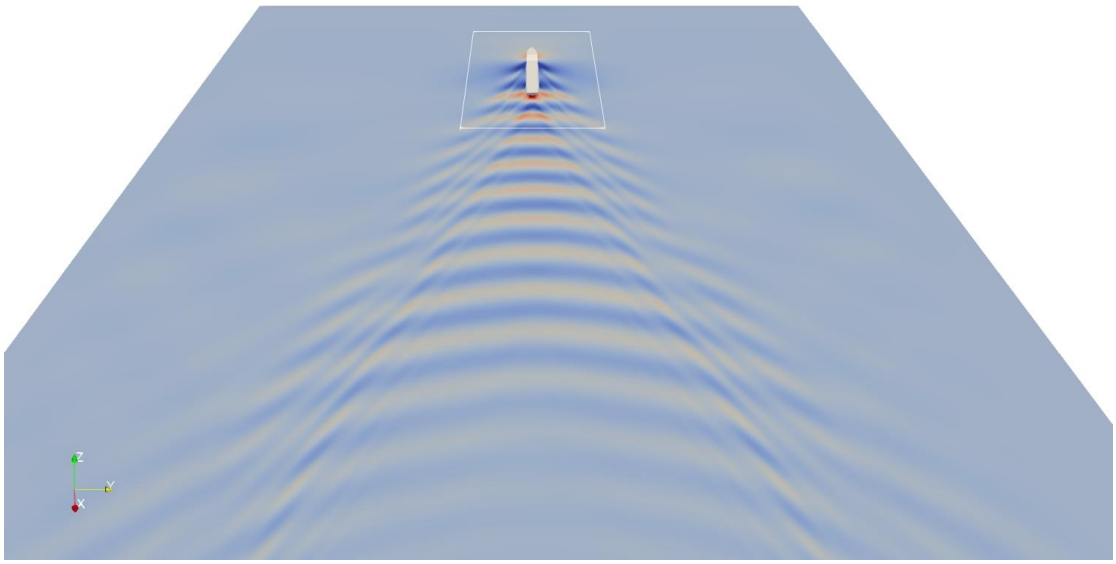

(a)

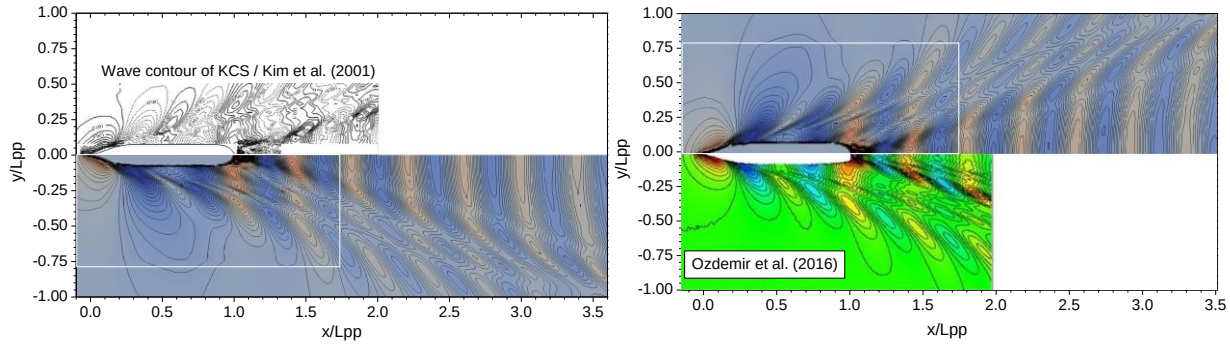

(b) (c)

Figure 14: Predicted wave pattern generated by KCS sailing in calm water and comparisons with previous measurement data and numerical results. (a) Wave pattern given by the proposed two-way

coupling method with medium mesh. (b) Top-half: measurement contours reported by Kim et al. (2001), bottom-half: present result. (c) Top-half: present result; bottom-half: numerical results reported by Ozdemir et al. (2016). The boundary of Ω_{OF} is indicated by the white box in all plots.

The wave cut profiles on x-z cut-planes at the three locations indicated in Figure 13 are compared with the measurement data of Kim et al. (2001) in Figure 15. The solutions on the three progressively refined meshes show obvious convergent behavior. The results of medium and fines meshes match well with experiment data. The wave profiles comparisons further reiterate the accuracy of the two-way coupling algorithm.

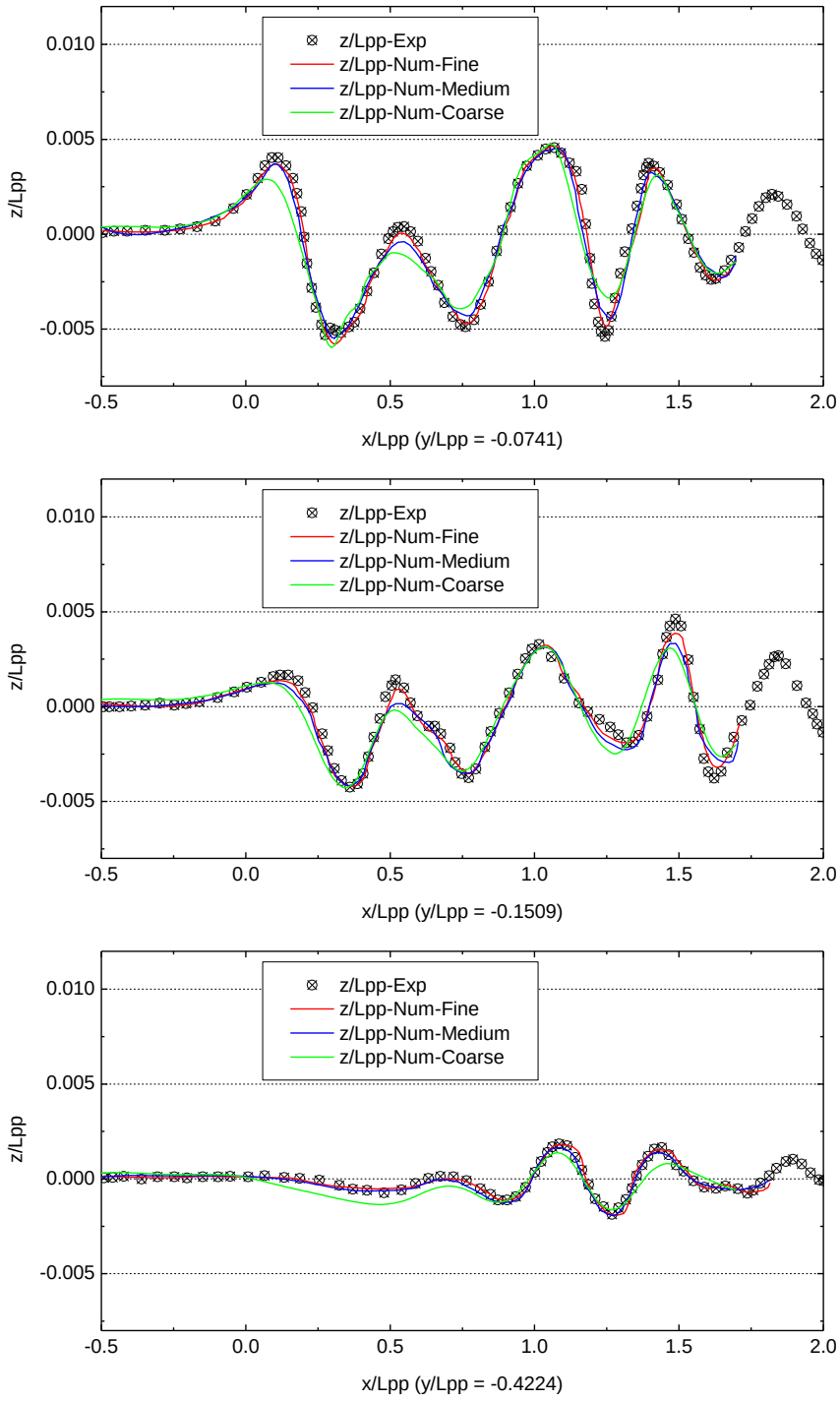

Figure 15: Wave profiles on cut planes at $y/L_{pp}=-0.0741$, -0.1509, and -0.4224 within Ω_{OF} (present CFD: solid lines; Measurements by Kim et al. (2001): symbols).

4 Conclusions

The paper presents a novel SCL method for the two-way coupling between a HOS-based potential flow solver and a FVM-based viscous flow solver. The design, the mathematical derivation, and the numerical implementation of the algorithm are described. Building upon the technical foundation of the

previously developed one-way coupling algorithm, the authors have introduced an innovative feedback mechanism from the viscous flow to the potential flow, enabling a seamlessly two-way coupling between the two solvers. As the algorithm primarily focused on simulating various wave phenomena, its main function is to assist the near-field viscous flow solver in receiving incoming wave information from the far field and then transmitting the new wave information calculated by the viscous flow solver back to the far field. During this process, eliminating the numerical errors generated in the viscous flow calculations before transmitting the information is vital in preventing the errors from accumulating over time.

The proposed method is tested by simulating 2D and 3D regular waves, as well as to simulating the wave generation due to a KCS ship sailing in calm water. In the 2D case, the coupled model can accurately reproduce the incident waves including wave height, phase, and kinematic features. The comparison at the outlet of the viscous domain was slightly less accurate but still within acceptable limits. In the more challenging 3D regular wave case, the current model maintained the incident waves with less wave distortion compared to the previous one-way coupling model. More importantly, the present model demonstrates excellent stability and convergence, with coupling errors and numerical diffusion errors in the viscous field not accumulating over time. In the case of KCS ship sailing in calm water, the model can perfectly propagate the near-field ship-generated waves to the far field, and comparisons of wave profile at different cut locations with measured date demonstrate the accuracy of the coupling.

These promising results provide a solid and efficient foundation for the simulations of more complex marine offshore applications in the future. In conventional CFD simulations of the hydrodynamic characteristics of structures in open seas, very large computational domains, together with spatially extended wave generation and absorption zones, are usually required to mitigate artificial sidewall effects, leading to a substantial increase in computational cost. In contrast, the SCL approach embeds a compact near-field viscous domain within a far-field HOS potential-flow model, enabling a significant extension of the effective computational domain while preserving high accuracy in the near field. As a result, the discretization burden associated with traditional CFD simulations is greatly reduced, and the overall computational efficiency is markedly improved.

The practical significance of SCL lies not only in its ability to minimize the artificial wall effects and significantly reduce computation time while using a compact viscous domain in the near field, but also extends beyond this. By retaining the feedback from the near field to the far field, one can achieve interactive numerical simulations between multiple near-field regions. Typical applications include simulating the influence of the wake of upstream floating platforms on downstream platforms in an offshore wind farm, as well as the mutual effects between two sailing ships, among others. Such simulation scenarios are unimaginable under traditional single computational domain viscous flow platforms due to the enormous computational resources required. With the help of the proposed SCL coupling method, achieving these simulations within an acceptable computational time could be realized.

As the final note, compared with one-way coupling, two-way coupling between potential and viscous flows requires additional stabilization measures. In Eq. (14), the relaxation factor α plays a key role, with α=0.025~0.05 found to provide robust stability and accuracy across a wide range of tests. For relatively simple cases, such as 2D/3D wave coupling with regular or irregular waves, this factor alone is sufficient. For moderately complex cases, e.g. wave interaction with stationary or slowly moving structures, further stabilization is achieved by applying a 7-point Savitzky–Golay filter to η_{HOS}' and ϕ_{HOS}', which preserves peaks, slopes, and signal details. For highly complex scenarios, such as coupling multiple fast-moving bodies in the near-field with a far-field wave field, strong coupling with multiple sub-iterations per time step is recommended, which can be implemented using external libraries such as *PreCICE (*Chourdakis G. *et al.(2022))*. This capability is planned as future work.

Credit Authorship Contribution Statement

Shi Kaiyuan: Writing – original draft, Methodology & Formulation, Coding. **Lu Xin**: Writing – original draft, review & editing, Supervision, Methodology, Coding, Validation, Visualization. **Dao My Ha**: Writing – review & editing, Technical discussion, Project supervision, Conceptualization of modelling framework. **Yulong Li:** Writing – review & editing, Technical discussion, Methodology. **Renchuan Zhu:** Writing – review & editing, Technical discussion, Methodology.

Declaration of Competing Interest

The authors declare that they have no known competing financial interests or personal relationships that could have appeared to influence the work reported in this paper.

Data availability

Data will be made available on request.

Acknowledgments

The work presented in this paper is a result of research conducted through the Enabling Future Systems for Offshore Wind Resources (ENFORCE) program, supported by A*STAR under its RIE 2025 Industry Alignment Fund (Grant No.: M23M4a0067). Author Kaiyuan Shi also gratefully acknowledges support from the Hainan Natural Science Foundation Youth Fund (Grant No. 525QN399) and the Natural Science Foundation of Shanghai (Grant No. 25ZR1402240).

References

[1] Aliyar, S., Ducrozet, G., Bouscasse, B., Sriram, V., Ferrant, P., 2022. Efficiency and accuracy of the domain and functional decomposition strategies for the wave-structure interaction problem. Ocean Eng. 266, 112568.

[2] Bateman, W.J.D., Swan, C., Taylor, P.H., 2003. On the calculation of the water particle kinematics arising in a directionally spread wavefield. J. Comput. Phys. 186, 70–92.

[3] Breuer, M., Jovičić, N., Mazaev, K., 2003. Comparison of DES, RANS and LES for the separated flow around a flat plate at high incidence. Int. J. Numer. Methods Fluids 41, 357–388.

[4] Chen, H., Wang, T., Greaves, D., Shi, H., & Zou, Q., 2025. A new CFD-MBD wave-structure interaction model: Coupling OpenFOAM with Chrono. *Applied Ocean Research, 165*, Article 104824. Advance online publication. https://doi.org/10.1016/j.apor.2025.104824.

[5] Chen, Y., Maki, K.J., 2017. A velocity decomposition approach for three-dimensional unsteady flow. Eur. J. Mech.-B/Fluids 62, 94–108.

[6] Choi, Y., Bouscasse, B., Seng, S., Ducrozet, G., Gentaz, L., Ferrant, P., 2018. Generation of regular and irregular waves in Navier-Stokes CFD solvers by matching with the nonlinear potential wave

solution at the boundaries, in: International Conference on Offshore Mechanics and Arctic Engineering. American Society of Mechanical Engineers, p. V002T08A020.

[7] Chourdakis G., Davis K., Rodenberg B., Schulte M., Simonis F., Uekermann B. et al., 2022. PreCICE v2: A sustainable and user-friendly coupling library [version 2; peer review: 2 approved]., Open Research Europe, 2:51.

[8] Deng, R., Ren, H., Li, H., Huang, S., Wu, T., 2024. Numerical study on the hydrodynamic performance of a high-speed taxiing fuselage: Investigation on the affecting factors in the numerical simulation. Ocean Eng. 309, 118499.

[9] Di Paolo, B., Lara, J.L., Barajas, G., Losada, ÍJ., 2021. Wave and structure interaction using multi-domain couplings for Navier-Stokes solvers in OpenFOAM. Part I: Implementation and validation. Coast. Eng. 164, 103799.

[10] Dommermuth, D.G., Yue, D.K.P., 1987. A high-order spectral method for the study of nonlinear gravity waves. J. Fluid Mech. 184, 267–288.

[11] Ducrozet, G., Bouscasse, B., Gouin, M., Ferrant, P. and Bonnefoy, F., 2019. CN-Stream: Open-source library for nonlinear regular waves using stream function theory. arXiv preprint arXiv:1901.10577.

[12] Ducrozet, G., Engsig-Karup, A.P., Bingham, H.B., Ferrant, P., 2014. A non-linear wave decomposition model for efficient wave–structure interaction. Part A: Formulation, validations and analysis. J. Comput. Phys. 257, 863–883.

[13] Ferrant, P., Gentaz, L., Alessandrini, B., Le Touzé, D., Nantes, E.C. de, 2003. A potential/RANSE approach for regular water wave diffraction about 2-D structures. Ship Technol. Res. 50, 165–171.

[14] Gao, J., Mi, C., Song, Z., Liu, Y., 2024. Transient gap resonance between two closely-spaced boxes triggered by nonlinear focused wave groups. Ocean Eng. 305, 117938.

[15] Gao, J., Wu, Y., Song, Z., He, M., 2026. Influences of low velocity uniform current on characteristics of gap resonance occurring between two adjacent fixed bodies. Mar. Struct. 106, 103961.

[16] Gong, S., Gao, J., Yan, M., Song, Z., Shi, H., 2025. Effects of floater motion on wave loads during steady-state gap resonance occurring between two non-identical boxes. Ocean Eng. 323, 120649.

[17] Gong, S., Gao, J., Song, Z., Shi, H., Liu, Y., 2024. Hydrodynamics of fluid resonance in a narrow gap between two boxes with different breadths. Ocean Eng. 311, 118986.

[18] Guo, B., Meng, J., Xie, Z., Ning, D. and Pan, S., 2025. A Lattice Boltzmann method for free surface flows over partially submerged structures. Computer Physics Communications 317, article number: 109852. (10.1016/j.cpc.2025.109852).

[19] Hamilton, J.A., Yeung, R.W., 2011. Viscous and inviscid matching of three-dimensional free-surface flows utilizing shell functions. J. Eng. Math. 70, 43–66.

[20] Hasselmann, K., Barnett, T.P., Bouws, E., Carlson, H., Cartwright, D.E., Enke, K., Ewing, J.A., Gienapp, A., Hasselmann, D.E., Kruseman, P. and Meerburg, A., 1973. Measurements of wind-

wave growth and swell decay during the Joint North Sea Wave Project (JONSWAP). Ergaenzungsheft zur Deutschen Hydrographischen Zeitschrift, Reihe A.

[21] Iafrati, A., Campana, E., 2003. A domain decomposition approach to compute wave breaking (wave-breaking flows). Int. J. Numer. Methods Fluids 41, 419–445.

[22] International Towing Tank Conference (ITTC), 2011. Practical Guidelines for Ship CFD Applications, in: Proceedings of the 26th International Towing Tank Conference. Brazil, pp. 1–18.

[23] Jacobsen, N.G., Fuhrman, D.R., Fredsøe, J., 2012. A wave generation toolbox for the open-source CFD library: OpenFoam. Int. J. Numer. Methods Fluids 70, 1073–1088.

[24] Jasak, H., 2009. OpenFOAM: Open source CFD in research and industry. International journal of naval architecture and ocean engineering, 1(2), 89–94.Kim, J., O'Sullivan, J., Read, A., 2012. Ringing analysis of a vertical cylinder by Euler overlay method, in: International Conference on Offshore Mechanics and Arctic Engineering. American Society of Mechanical Engineers, pp. 855–866.

[25] Kim, S.-H., Yamashiro, M., Yoshida, A., 2010. A simple two-way coupling method of BEM and VOF model for random wave calculations. Coast. Eng. 57, 1018–1028.

[26] Kim, W., Van, S., Kim, D., 2001. Measurement of flows around modern commercial ship models. Exp. Fluids 31, 567–578.

[27] Lachaume, C., Biausser, B., Fraunié, P., Grilli, S.T., Guignard, S., 2003. Modeling of breaking and post-breakingwaves on slopes by coupling of BEM and VOF methods, in: ISOPE International Ocean and Polar Engineering Conference. ISOPE, pp. ISOPE–I.

[28] Landesman, P., Harris, J.C., Peyrard, C., Benoit, M., 2024. Wave–structure interaction by a two–way coupling between a fully nonlinear potential flow model and a Navier–Stokes solver. Ocean Eng. 308, 118209.

[29] Larsen, B.E., Fuhrman, D.R., 2018. On the over-production of turbulence beneath surface waves in Reynolds-averaged Navier–Stokes models. J. Fluid Mech. 853, 419–460.

[30] Larsson, L., Stern, F., Visonneau, M., 2013. Numerical ship hydrodynamics: an assessment of the Gothenburg 2010 workshop. Springer.

[31] Li, Y., Law, Y.Z., Joshi, V., Jaiman, R.K., 2018a. A 3d common-refinement method for non-matching meshes in partitioned variational fluid–structure analysis. J. Comput. Phys. 374, 163–187.

[32] Li, Y., Su, M., Li, H., Deng, R., Wang, K., Hu, Z., 2019. Numerical research on time domain ship motions coupled with sloshing at different liquid levels and forward speeds. Ocean Eng. 178, 246–259.

[33] Li, Y., Zhu, R., Miao, G., Fan, J., 2012. Simulation of tank sloshing based on openfoam and coupling with ship motions in time domain. J. Hydrodyn. 24, 450–457.

[34] Li, Z., Bouscasse, B., Ducrozet, G., Gentaz, L., Le Touzé, D., Ferrant, P., 2021. Spectral wave explicit Navier–Stokes equations for wave-structure interactions using two-phase computational fluid dynamics solvers. Ocean Eng. 221, 108513.

[35] Li, Z., Bouscasse, B., Gentaz, L., Ducrozet, G., Ferrant, P., 2018b. Progress in coupling potential wave models and two-phase solvers with the SWENSE methodology, in: International Conference on Offshore Mechanics and Arctic Engineering. American Society of Mechanical Engineers, p. V009T13A027.

[36] Lin, P., 2008. Numerical modeling of water waves. CRC Press.

[37] Lu, X., Chandar, D.D.J., Chen, Y., Lou, J., 2017. An overlapping domain decomposition based near-far field coupling method for wave structure interaction simulations. Coast. Eng. 126, 37–50.

[38] Lu, X., Dao, M.H., Le, Q.T., 2022. A GPU-accelerated domain decomposition method for numerical analysis of nonlinear waves-current-structure interactions. Ocean Eng. 259, 111901.

[39] Luo, W., Jiang, D., Wu, T., Liu, M., Li, Y., 2022. Numerical simulation of the hydrodynamic characteristics of unmanned underwater vehicles near ice surface. Ocean Eng. 253, 111304.

[40] Mi, C., Gao, J., Song, Z., Liu, Y., 2025a. Hydrodynamic wave forces on two side-by-side barges subjected to nonlinear focused wave groups. Ocean Eng. 317, 120056.

[41] Mi, C., Gao, J., Song, Z., Yan, M., 2025b. Gap resonance between a stationary box and a vertical wall induced by transient focused wave groups. China Ocean Eng. 39(3), 441-454.

[42] Ozdemir, Y.H., Cosgun, T., Dogrul, A., Barlas, B., 2016. A numerical application to predict the resistance and wave pattern of KRISO container ship. Brodogradnja: Int. J. Nav. Archit. Ocean Eng. Res. Dev. 67, 47–65.

[43] Peltonen, P., Kanninen, P., Laurila, E., Vuorinen, V., 2020. The ghost fluid method for OpenFOAM: A comparative study in marine context. Ocean Eng. 216, 108007.

[44] Schroeder, W., Martin, K.M. and Lorensen, W.E., 1998. The visualization toolkit an object-oriented approach to 3D graphics. Prentice-Hall, Inc.

[45] Shao, Y.-L., Faltinsen, O.M., 2014. A harmonic polynomial cell (HPC) method for 3D Laplace equation with application in marine hydrodynamics. J. Comput. Phys. 274, 312–332.

[46] Shi, K., Zhu, R., 2023. Efficient spectral coupled boundary element method for fully nonlinear wave–structure interaction simulation. Phys. Fluids 35.

[47] Tang, K., Wang, J., Chen, X., Jiang, D., Li, Y., 2021. Nonlinear ship motion with forward speed in waves based on 3d time domain hybrid green function method. Eng. Anal. Bound. Elem. 123, 107–121.

[48] Yu, J., Yao, C., Zhou, Y., Dong, G., Zhang, Z., Feng, D., 2024. A hybrid numerical framework of potential and viscous flows for simulations of free running surface ship maneuvering in waves. Ocean Eng. 301, 117465.

[49] Zhang, J., Guo, H., Tang, Y., Li, Y., 2020. Effect of top tension on vortex-induced vibration of deep-sea risers. J. Mar. Sci. Eng. 8, 121.

[50] Zhao, J., Zhu, R., Zhou, W., 2022. Implementation of a velocity decomposition method coupled with volume-of-fluid method for simulating free-surface flows. Ocean Eng. 263, 112339.

[51] Zhuang, Y., Wan, D., 2021. Parametric study of a new HOS-CFD coupling method. J. Hydrodyn. 33, 43–54.

[52] Zou, Q. P., Chen, Y., Cluckie, I., Hewston, R., Pan, S., Peng, Z., & Reeve, D., 2013. Ensemble prediction of coastal flood risk arising from overtopping by linking meteorological, ocean, coastal and surf zone models. Quarterly Journal of the Royal Meteorological Society, 139(671), 298-313. https://doi.org/10.1002/qj.2078